nuclear fusion
IAEA

PAPER • OPEN ACCESS

Overview and current status of the IFMIF-DONES accelerator systems

To cite this article: I. Podadera *et al* 2025 *Nucl. Fusion* **65** 122011

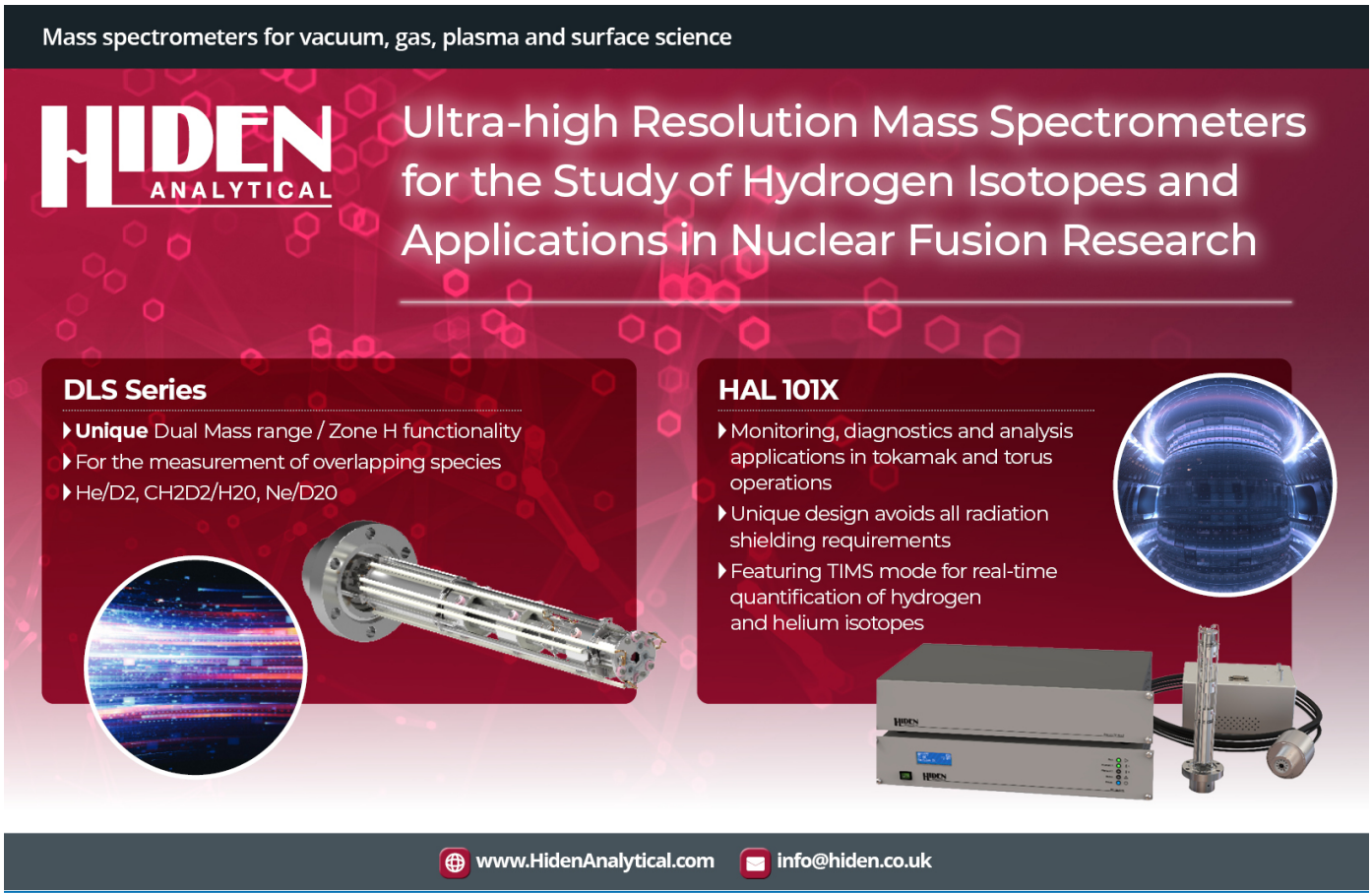

OPEN ACCESS
IOP Publishing | International Atomic Energy Agency
Nuclear Fusion
Nucl. Fusion **65** (2025) 122011 (30pp)
https://doi.org/10.1088/1741-4326/ade267

Overview and current status of the IFMIF-DONES accelerator systems

I. Podadera[1,*], P. Cara[2], B. Bolzon[3], C. Caballero[1], N. Chauvin[3], M. Comunian[4], D. Cosic[5], M. Eshraqi[6], M.J. Ferreira[6], V. Hauer[7], D. Jiménez-Rey[8], L. Macià[9], A. Madur[3], J. Marroncle[3], P. Méndez[8], M. Montis[4], C. de la Morena[8], C. Oliver[8], A. Palmieri[4], J. Plouin[3], A. Pisent[4], D. Poljak[10], D. Regidor[8], A. Sabogal[11], L. Seguí[3], A. Šušnjara Nejašmić[10], T. Tadic[5], K. Tomić Luketić[5], C. Torregrosa[1], A. Ibarra[1,8] and the EUROfusion WPENS Team[a]

[1] IFMIF-DONES España, Granada, Spain
[2] Fusion for Energy, Barcelona, Spain
[3] IRFU-CEA, Université Paris-Saclay, Gif-sur-Yvette, France
[4] INFN, Legnaro, Italy
[5] Ruder Boskovic Institute, Zagreb, Croatia
[6] Lund University, Lund, Sweden
[7] Karlsruhe Institute of Technology, Karlsruhe, Germany
[8] CIEMAT, Madrid, Spain
[9] IREC, Barcelona, Spain
[10] University of Split, Split, Croatia
[11] University of Granada, Granada, Spain

E-mail: ivan.podadera@ifmif-dones.es

Received 31 October 2024, revised 27 April 2025
Accepted for publication 9 June 2025
Published 30 September 2025

Abstract

The IFMIF-DONES facility provides a very high intensity flux of neutrons for research on materials of future fusion reactors and other complementary applications. The generation of those neutrons is driven by stripping reactions between energetic deuteron particles and a liquid lithium jet. The requirements on the deuteron beam are to deliver a 40 MeV beam with a constant current of 125 mA. All the systems involved in the generation, acceleration, transport and shaping of the deuteron beam are grouped in the so-called accelerator systems (AS). The design of this high-power driver has been ongoing for a long time, and many prototypes of the critical technologies have been tested. During the last decade, the design has been consolidated and evolved into an engineering design ready for construction. The overview of the main features of the design and the current status is presented in this article.

Keywords: particle accelerator, nuclear fusion, materials, radiofrequency, superconducting LINAC's

(Some figures may appear in colour only in the online journal)

[a] See the Appendix in Ibarra *et al* (https://doi.org/10.1088/1741-4326/adb864) for the EUROfusion WPENS Team.
[*] Author to whom any correspondence should be addressed.

1. Introduction

IFMIF-DONES [1, 2] is a research infrastructure under construction in Granada, Spain, with the main goal of irradiating the candidate materials for their use in future fusion reactors. An irradiation damage similar to the one produced by fusion reactors is replicated experimentally with the bombardment of neutrons produced at stripping reactions between a high-energy deuteron beam at 40 MeV and a liquid lithium curtain. Combined with a high number of impinging deuterons provided by an intense current of 125 mA, this produces a high rate damage in the materials samples near the lithium target, of up to 20 dpa yr^{-1}, and a production of helium and hydrogen within the materials similar to those of the future fusion reactors.

1.1. Design background

The IFMIF-DONES accelerator based its design on the grounds of the IFMIF accelerator, which was developed since the start of this century in a bunch of projects. In particular, a one-to-one mock-up of the front-end section of the accelerator has been carrying out validation within the IFMIF/EVEDA project of the Broader Approach collaboration between Europe and Japan [3], the so-called Linear IFMIF Prototype Accelerator, LIPAc [4]. The configuration of the accelerator is first given by the plant requirements, which ask to provide a neutron flux sufficient to cause a damage equivalent to more than 20 dpa_{NRT} in less than 2.5 yr in a volume of 0.3 dm^3, or 50 dpa_{NRT} in 3 yr in a volume of 0.1 dm^3, just after impinging the liquid lithium target.

After optimization of the design along the years, the energy of the deuterons interacting with the lithium was set to 40 MeV, and the average beam current of 125 mA. Regarding the beam-on-target (BOT) profile, a nominal beam profile of 20 cm in horizontal and 5 cm in vertical has been used as a reference. An specific discussion on the influence and sensitivity of those parameters can be found in [5]. The main parameters of the accelerator are listed in table 1.

During the start of the IFMIF project design, the experience operating accelerators at the multi-MW power level around the world was scarce. However, the recent years have boosted the limit of the intensity frontier at low energies, pushed by the necessities of neutron sources and ADS (Accelerator-driven subcritical systems) [6] facilities. Figure 1 shows the high power hadron accelerators under design, under commissioning and the already operational. The present record is at SNS SC LINAC, where a beam of 1.7 MW is operated routinely, with plans to increase it further to 2.8 MW with a new second target station [7]. Many projects are now under commissioning which are designed for a similar range of operation, such as ESS or CiADS. In the low-energy high-intensity CW regime, the old test accelerator LEDA has still the record, with 670 kW achieved using a 100 mA CW proton beam from an Radio Frequency Quadrupole (RFQ) with an output energy of 6.7 MeV. Nevertheless in the very recent years, CAFE has reported almost 200 kW [8], using a room temperature front-end based on an RFQ, and four cryomodules in a similar configuration to IFMIF-DONES, accelerating a CW 10 mA proton beam up to ca. 20 MeV for more than 10 h. SPIRAL2 has also reported exciting results with a deuteron beam at the same energy as IFMIF-DONES, 40 MeV. In this case, they accelerated around 16 kW of deuteron beam, corresponding to 5 mA at an energy of 33 MeV, but in pulsed mode due to safety limitations. However, the limit was more imposed by safety licensing than by the accelerator operation and could have increased the duty cycle up to the CW design regime and the hundreds of kW. Last but not least, the LIPAc accelerator, prototype of the front-end of IFMIF-DONES, accelerated very recently ca. 120 mA up to 9 MeV, at a duty cycle of 8.75%, resulting in around 50 kW of average beam power transported down to a high power beam dump [9]. Together with the validation during the previous phases, it gave very important hints of many of the IFMIF-DONES systems, such as the injector, the RFQ, the Medium Energy Beam Transport Line (MEBT), the Radio Frequency Power System (RFPS), the ancillaries or the High Energy Beam Transport line (HEBT) including the High Power Beam Dump (HPBD).

Table 1. Main beam accelerator systems nominal parameters. I_{peak} is the peak current, DC is the beam duty cycle, E_f is the final particle kinetic energy, P_f is the final beam power, f_0 the bunch frequency, $S_{BOT,x}$ is the nominal horizontal size of the beam-on-target and $S_{BOT,y}$ the vertical one.

Particle	D^+(p)
IO_{peak}	125 mA
DC	CW
E_f	40 ± 5 MeV FWHM
P_f	5 MW
f_0	175 MHz
$S_{BOT,x}$	10–20 cm
$S_{BOT,y}$	5 cm

2. Accelerator design

The main parameter driving all the aspects of the design of the IFMIF-DONES accelerator is the high availability requested to the whole facility, 70%, which translates to a overall availability for the accelerator systems (ASs) of 87% [10]. This has huge implications in the way the systems are maintained, as the Mean-Time-To-Repair (MTTR) should be kept to a minimum, while Mean-Time-To-Failure (MTTF) increased as much as possible.

Using the knowledge acquired from the previous designs and prototypes, the current design of the IFMIF-DONES accelerator is a LINAC with three main stages (see figures 2 and 3): (1) a normal conducting front-end where the deuteron (or proton) beam is generated, injected at 100 keV into a normal conducting RFQ accelerating the particles up to an individual kinetic energy of 5 MeV ($\beta = 0.07$); (2) a small transport line at medium energy (MEBT) matching the beam with

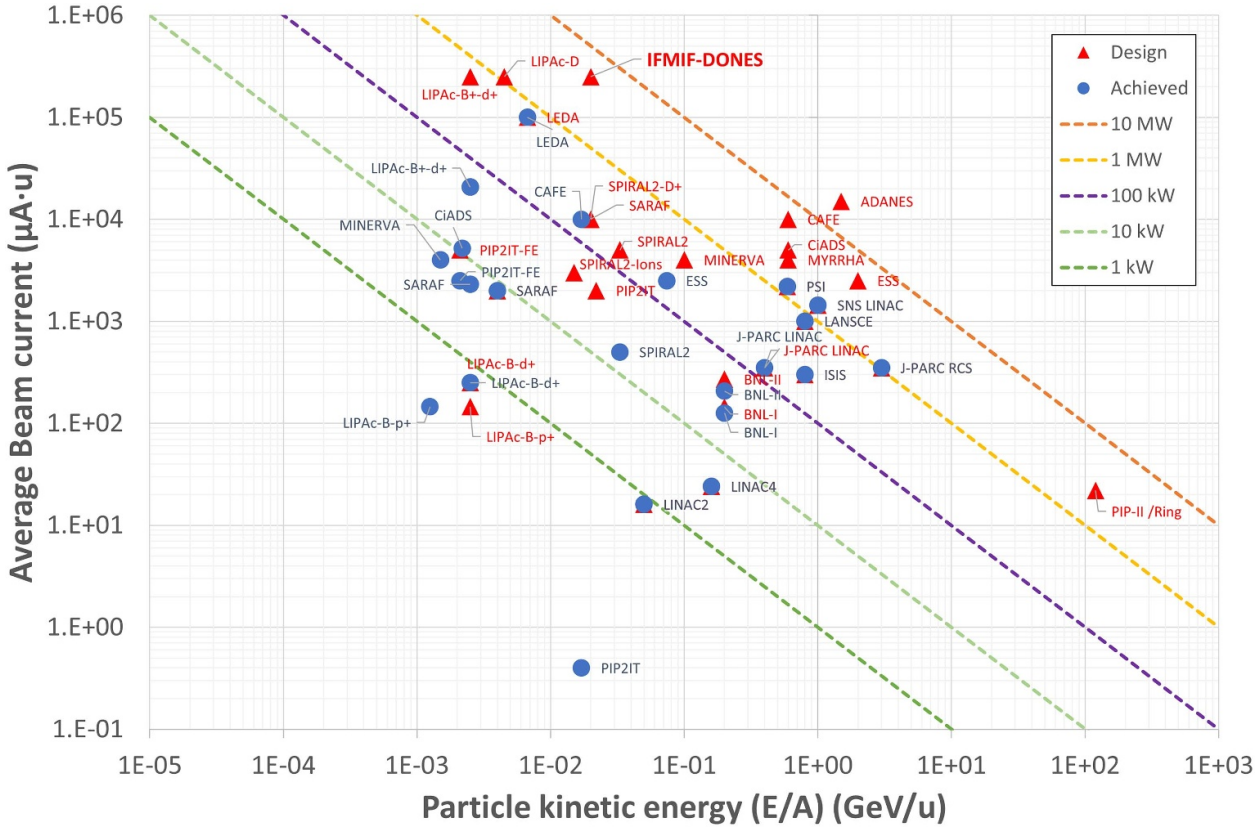

Figure 1. Landscape of foreseen and current status of high power hadron accelerators around the world.

the input parameters of a superconducting radio frequency LINAC (SRF LINAC), which brings the particle beam to the final kinetic energy of 40 MeV; and (3) a HEBT line transporting the beam down to the target and shaping and controlling the BOT parameters.

The 49 RF resonant cavities (1 RFQ, 2 re-buncher cavities and 46 superconducting cavities) are powered by solid-state RF power amplifiers.

The starting point for the whole accelerator design is the beam physics design (section 2.1), supported mainly by TraceWin simulations [11]. This provides the input for the systems design (section 3), which is complemented by other machine transversal studies, such as beam pipe vacuum (section 2.2), control systems (section 2.3) or commissioning studies (section 2.4). Each of these points are further developed hereafter.

2.1. Beam physics

The primary objective of the IFMIF-DONES accelerator is to generate a 125 mA continuous deuteron beam, accelerate it to an energy of 40 MeV, and transport and finally shape this beam to optimize its interaction with the lithium neutron converter. While doing so, one has to minimize beam losses in the accelerator, as power deposition can be harmful and the accelerator components could be activated. The final beam power of the IFMIF-DONES accelerator reaches an unprecedented level of 5 MW. Besides, the beam power exceeds 1 MW throughout a substantial portion of the accelerator (after the first cryomodule, see section 2.1.5). In order to maintain power losses within the target range of around a watt per meter, losses shall be kept below 1×10^{-6} of the total beam power. Moreover, the beam transport throughout the entire DONES accelerator is performed under a high space charge regime. Space charge refers to the repulsive forces between charged particles of the same sign, which are in general, non-linear and can deteriorate the beam quality. The criteria to quantify the space charge is the generalized perveance, K, defined as:

$$K = qI/2\pi\epsilon_0 m_0 \beta\gamma c^3 \tag{1}$$

where I is the beam intensity, q and m_0 represent the charge and rest mass of the particles, ϵ_0 is the vacuum permittivity, γ is the Lorentz factor and β is the ratio of particle's velocity to the speed of light in vacuum. Due to the high intensity of the IFMIF-DONES beam (in the numerator of equation (1)) and its relatively low energy (in the denominator of equation (1)), the perveance reaches the highest values among existing or planned megawatt-class linacs (such as SNS, ESS or J-PARC, for instance) [12]. Consequently, the beam is expected to be submitted to strong space charge forces which often dominate the focusing forces. The beam physics, simulations, and accelerator design for DONES were mainly driven by the unprecedented challenges arising from the simultaneous combination of extremely high intensity and power [13]. The accelerator design began in the late 2000s in the framework of the IFMIF

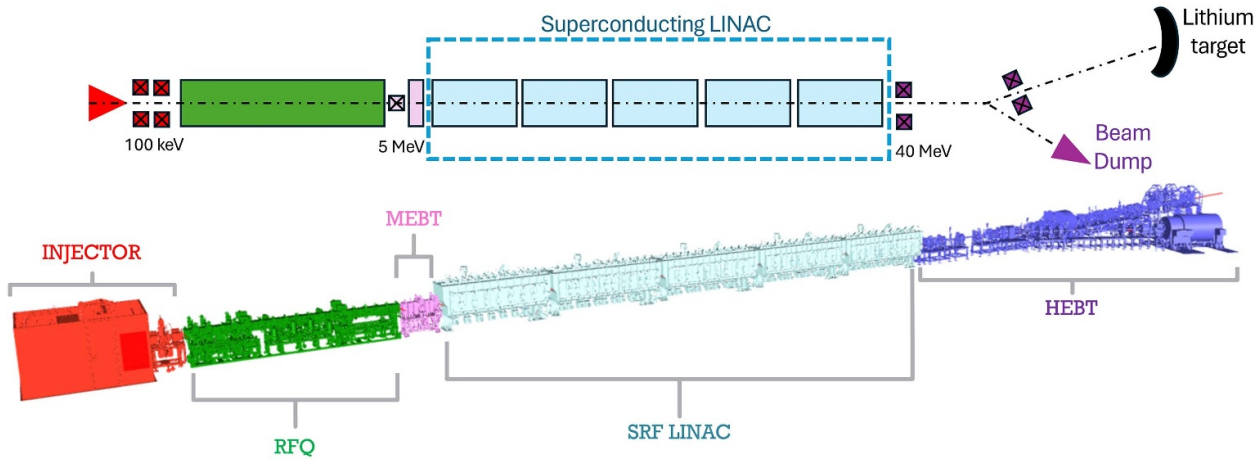

Figure 2. Layout and mockup of the IFMIF-DONES accelerator beamline.

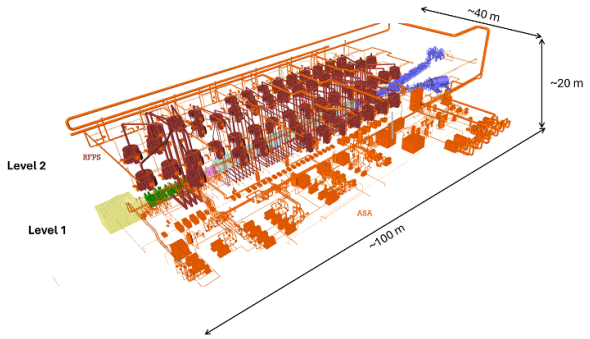

Figure 3. The configuration of the systems of the IFMIF-DONES accelerator inside the main building including its ancillaries (ASA) and the RFPS. Systems are spread among three floor levels: RFPS and LICS (not shown) in Level 2, accelerator line and ancillaries in Level 0, and experimental lines in Level -1 (not shown).

project. Since then, it has undergone significant evolution, particularly the superconducting linac and high-energy beam line, to meet new requirements and engineering design constraints. The final layout of the accelerator (see figure 4) is as follows (each accelerator part will be detailed in the next sections):

- An ECR ion source generates D^+ ions, which are extracted by a five-electrode system that accelerates the particles to 100 keV.
- A Low Energy Beam Transport (LEBT) line focuses the beam with solenoids and adapts it to optimize its injection into the RFQ.
- A RFQ provides strong transverse focusing while bunching and accelerating the beam to the energy of 5 MeV.
- A Mean Energy Beam Transport (MEBT) line focuses the beam transversally with quadrupoles and longitudinally with rebuncher, in order to adapt it for its injection into the SRF LINAC.
- A SRF LINAC, composed of 5 cryomodules, focuses the beam with solenoids and accelerates it with Half-Wave-Resonator cavities up to the energy of 40 MeV.
- A HEBT line focuses the beam with quadrupoles, bends it with two dipoles, homogenizes the beam density using higher-order multipoles, and expands and shapes it to the required size and profile at the target.

2.1.1. Source extraction system. A beam extraction system, consisting of a set of electrodes, is designed to extract D^+ particles from the ECR ion source plasma and accelerate them to 100 keV. To anticipate a potential transmission of the injector-RFQ sections of around 90%, 140 mA of D^+ has to be extracted. As a D^+ fraction of around 85% is expected in the low energy beam, a total extracted current from the source of 165 mA, including molecular ions D^{2+} and D^{3+} ions is targeted. The input beam emittance must remain below $0.30\,\pi$ mm · mrad (with a target value of $0.25\,\pi$ mm · mrad) at the RFQ entrance, after the transport through the LEBT, to ensure good transmission. High current and low emittance often present conflicting requirements, particularly at low energy. Since the beam, and consequently its emittance, is generated by the ion source, the extraction system has to be carefully designed and studied. Various extraction configurations have been investigated [14], including variations in electrode number, aperture diameter, geometry, and voltage. Beam extraction system and particle trajectories have been calculated using the AXCEL [15] code and, more recently, with IBSimu [16].

2.1.2. Low energy transport line. The LEBT utilizes a dual solenoid focusing scheme to transport the beam and match it in order to optimize its injection into the RFQ. In order to keep the LEBT as short as possible, horizontal and vertical magnetic dipole correctors are inserted inside each solenoid. The total beamline length, from the plasma electrode to the inner face of the RFQ entrance flange, measures 2.05 m (see figure 5). At the end of the LEBT, a cone is positioned just before RFQ injection, allowing the injection of the D^+ beam while blocking other species (D^{2+} and D^{3+}) that are extracted from the source and transported through the line.

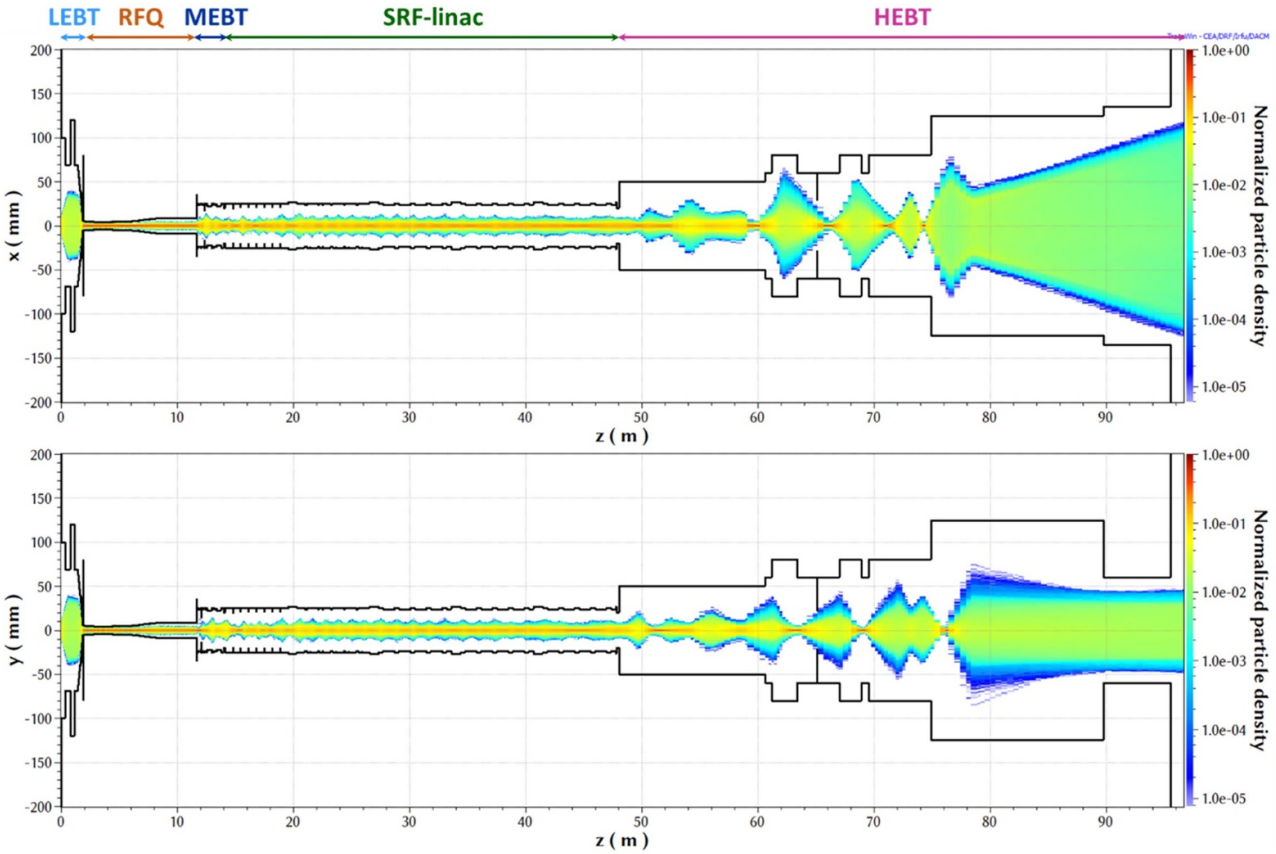

Figure 4. Beam density in the transverse x and y planes along the IFMIF-DONES accelerator.

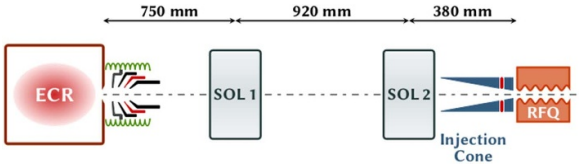

Figure 5. IFMIF-DONES LEBT layout.

Beam transport in such a LEBT operates under a space charge compensation regime. This phenomenon has been thoroughly studied [17, 18] using self-consistent PIC codes like WARP [19], which take into account secondary particle generation through collision processes, but require a lot of CPU time. To incorporate space charge compensation into tracking codes such as Tracewin [11], a model outlined in [20], based on a semi-empirical approach developed by Gabovitch, is used. This model preserves a certain level of self-consistency by computing the space charge compensation degree along the beam line considering, mainly, the beam radius, beam current and vacuum level. Simulation results from this LEBT model have shown good agreement with those obtained using PIC codes, as well as with experimental data from the LIPAC injector [21].

2.1.3. Medium energy acceleration. After being extracted from the ion source and focused by the LEBT, the beam is accelerated by a RFQ resonant cavity up to an energy of 2.5 MeV u^{-1}. The beam physics design of the RFQ is composed of an RMS, Shaper, Gentle Buncher (three meters long), and an Accelerator (around 7 m long) [22]. The main points of the design include the use of the standard LANL chain of RFQ Codes: Curl, RFQuick, Pari, Parmteqm, and Vanes [23]. This allows for very fast feedback on the full multiparticle response to every parameter variation studied in the RFQ. An important aspect of the design is using an analytic law on voltage shape (equation (2)), which can increase the voltage smoothly in the accelerator part, as seen in [24]. The average aperture R_0 follows the same law to keep the surface field under control. The maximum emittance, i.e. acceptance, in the accelerator part has been increased to reduce losses at high energy. The RFQ design has a high value of focusing factor B, to keep the beam in the linear part of the focusing fields [25]. In table 2 the main RFQ parameters are listed.

$$V(z) = V_1 + (V_2 - V_1) \times \left[\frac{1}{2} + \frac{15}{8}\left(-\sin\delta z_{12} - \frac{1}{3}\sin 3\delta z_{12} + \frac{1}{5}\delta z_{12}\right)\right] \quad (2)$$

$$R_0(z) = R_{01} + (R_{02} - R_{01}) \times \left[\frac{1}{2} + \frac{15}{8}\left(-sin\delta z_{34} - \frac{1}{3}\sin 3\delta z_{34} + \frac{1}{5}\delta z_{34}\right)\right] \quad (3)$$

Table 2. Main parameters of the IFMIF-DONES RFQ.L is the total length of the RFQ, f_0 the resonance frequency, I_i the input deuteron current, V_{min} and V_{max} the minimum and maximum voltage respectively, E_i and E_o the input and output beam kinetic energy respectively and $E_{s,max}$ the maximum surface electric field.

L	9.78 m (5.7 λ)
f_0	175 MHz
I_i	130 mA
V_{min}/V_{max}	79.29/132 kV
E_i/E_o	0.1/5 MeV
$E_{s,max}$	25.2 MV m^{-1} (1.8 kp)

with $\delta z_{12} = \frac{\pi}{6} - \frac{\pi(z-z_1)}{3(z_2-z_1)}$ and $\delta z_{34} = \frac{\pi}{6} - \frac{\pi(z-z_3)}{3(z_4-z_3)}$.

2.1.4. Medium energy transport. The role of the MEBT section is essential for a proper beam transport from the RFQ and an optimized injection into the SRF LINAC. It consists of two beam scrapers (horizontal and vertical) to limit the beam halo, two buncher cavities (five-gap IH resonators with a β of 0.073) operating at 175 MHz, and five magnetic quadrupoles, all within a total length of 2.35 m. Five quadrupoles are needed for matching the beam size and divergence in the two transverse plane, and managing its extent throughout the MEBT.

2.1.5. High energy acceleration. The acceleration and transport of high-intensity beams necessitates both a large beam pipe aperture and a conservative accelerating field to minimize beam losses and reduce RF power demands. However, a larger aperture increases the peak-to-accelerating field ratio, which in turn requires lowering the accelerating gradient to maintain the peak surface field within acceptable limits. Consequently, an accelerating gradient below 4.5 MV m^{-1} and apertures in the 40–50 mm range were selected for the superconducting resonators. Two resonator families, each with different geometric β-values, are sufficient to handle the acceleration from the RFQ exit at 5 MeV to the final energy of 40 MeV. An initial SRF LINAC layout, with four cryomodules, was initially developed in the framework of the IFMIF project [26]. However, during the development of the SRF cavities, new frequency tuners had to be designed, resulting in each cavity being 100 mm longer than originally planned. Beam dynamics studies showed that initial IFMIF SRF LINAC design (with four cryomodules) with the cavity additional lengths lead to beam losses above the requirements. Consequently, a new SRF LINAC layout was proposed, aiming for a less aggressive synchronous phase law, in order to increase the longitudinal acceptance and a higher transverse phase advance per meter. As a result, the final DONES SRF LINAC is composed by five cryomodules:

- the first cryomodule contains eight periods of one solenoid and one resonator ($\beta_{opt} = 0.115$).
- the second cryomodule contains five periods of one solenoid and one resonators ($\beta_{opt} = 0.115$) and ends with one solenoid and one resonator.
- the last three cryomodules, which are identical, contain four periods of one solenoid and two resonators ($\beta_{opt} = 0.175$) and ends with one solenoid and one resonator.

The total length of the SRF LINAC, as shown in figure 1, is 32.67 m. With a beam intensity of 125 mA, the maximum RF power per cavity is 75 kW for the low-β resonators and 150 kW for the high-β resonators. The axial field induced by the superconducting solenoids is maintained at approximately 6 T to allow the use of conventional NbTi technology for the coils. The solenoid package includes bucking coils to cancel fringe fields at the cavity location, as well as steering coils paired with button-type BPMs for orbit correction.

The beam dynamics studies performed to validate the MEBT and SRF LINAC design were conducted using TraceWin [11]. The magnetic fields generated by the solenoid and resonators were modeled using 3D field maps calculated by finite element method.

In a high-intensity, high-power accelerator like IFMIF-DONES, the primary objective is to transport the beam while minimizing its halo to prevent beam losses and meet hands-on machine requirements. Since the beam is directed onto a neutron production target, the final emittance is no longer the main figure of merit. Therefore, in the MEBT and SRF LINAC sections, beam tuning is performed using a 'halo matching' method, which smooths the outer boundary of the beam, reduces halo formation [26], and ultimately minimize potential beam losses. This approach minimizes the radial spread of the outermost macro-particles, particularly at focusing elements, by optimizing the entire lattice with a particle swarm optimization algorithm [27].

The beam was simulated using 1×10^6 macro-particles, the minimum required to have enough statistic in order to ensure that beam losses remain below 1 W m^{-1}, as specified. This implies that fewer than one particle over 1×10^6 can be lost, a phenomenon referred to as 'micro-losses.' The simulation and optimization method can be directly applied to the real accelerator during its commissioning and operational phases. The process relies on beam diagnostics that will be available in the actual machine, specifically micro beam loss monitors (μBLMs) (see section 3.6.1). These detectors will be placed at each period, close to the beam, to provide independent data collection for micro-losses minimization by adjusting focusing forces.

2.1.6. High energy transport and shaping. The HEBT is designed to safely transport the beam from the SRF to the target and shape it to meet strict size and uniformity requirements. A summary of the main beam specifications is presented in table 3. Variable beam size in the horizontal direction (10–20 cm), side peaks and general beam distribution are required to provide additional flexibility for neutron irradiation [5].

The use of non-linear magnets has been chosen as the method to achieve the required rectangular uniform beam profile at the target. This aligns well with the features of DONES, particularly in terms of high beam power and the use of a

Table 3. New beam on-target requirements [5]. E_f is the particle kinetic energy, $S_{x,90}$ the horizontal size containing 90% of the particles, $PD_{av,90}$ the power density containing 90% of the particles, PD_{max} the maximum power density, α the beam incidence angle on the target, $\delta x, y$ the beam position accuracy an s_{max} the maximum horizontal beam extension.

E_f	(40.0 ± 0.5) MeV
$S_{x,90}$	10–20 cm (16.6 cm reference)
$PD_{av,90}$	480 W mm^{-2}
PD_{max}	$<$700 W mm^{-2} ($v_{Li} = 15$ m s^{-1})
α	9 deg
$\delta x, y$	$\pm$5 mm
Tails	$\leqslant$0.2 W mm^{-2} $>$ 22 cm
Side peaks (hor)	$\leqslant$30% average current density
$s_{x,max}$	25 cm

liquid target. It is based on modifying the transverse velocity of particles by using a nonlinear magnetic field that depends on the transverse coordinates. While particles in the center of the beam distribution remain unaffected by the non-linear magnetic field, the divergence of particles far from the center is modified so that after subsequent transport, the beam edges are folded into the core. Octupoles are primarily responsible for producing the uniform distribution, whereas the main purpose of the dodecapoles, located upstream of the octupoles, is to independently manage beam halo particles. The design of the HEBT has been determined by challenging conditions such as beam power, space charge conditions, and continuous operation mode. The final layout has been optimized to provide a flexible and operational line, resulting from a compromise between beam dynamics, beam diagnostics, radioprotection issues, and component design and integration requirements. The layout of the HEBT can be seen in figure 26.

The particles are guided through the nearly 49 m long HEBT using 18 resistive quadrupoles. A bend of 9° relative to the main accelerator axis has been implemented to balance maximizing the high flux volume in the test cell (TC) (using smaller angles) and minimizing machine activation due to neutron back-streaming into the active beam line components (using larger angles) [28]. Non-linear magnets (two octupoles and dodecapoles) are included for beam shaping. During beam commissioning, the beam will be deviated to the so-called Beam Dump Transport line (BDTL) through a 34.5° bending magnet, followed by 6 quadrupoles to adapt the beam to the beam dump requirements. A residual bunch beam extraction has been incorporated for additional experiments on the lower floor.

In the HEBT layout, we can identify three main functional sections from the perspective of beam dynamics.

- HEBT-S1: this first section of the transport line aims to reduce the backward radiation from the target on the upstream accelerator components. A quasi-achromat system composed of two 4.5° dipoles with a quadrupole to minimize beam dispersion has been considered. Six quadrupoles positioned upstream of the dipoles are required to adapt the beam from the SRF to specific conditions at the entry of the second section. In addition, two residual extraction lines are integrated into this section: one for commissioning activities, which goes through the BDTL, and the other for experimental activities, which extracts residual bunches to the ground floor.
- The beam shaping by using non-linear magnetic fields (octupoles and dodecapoles magnets) is introduced in the next section, HEBT-S2. The use of these non-linear magnets allows for the shaping of the beam phase space by folding the beam tails and modifying it from a quasi-Gaussian beam to a more rectangular beam profile as required in the target. To shape the beam with such high-order fields, a specific linear optics arrangement is needed. One direction of the beam profile needs to be enlarged while the other needs to be very small to reduce transverse coupling. To achieve this, a quadrupole triplet is placed before the pair of non-linear magnets to ensure proper beam evolution in the octupoles or dodecapoles.
- Finally, the third section, HEBT-S3, matches the phase advance and beam size to the target requirements by using the last six quadrupoles.

Given the high beam power combined with the halo production caused by the strong space charge regime and the non-linear magnets shaping implementation, potential beam losses are safely concentrated in specific elements installed in the HEBT line. Water-cooled mobile scrapers are integrated among dodecapoles to effectively remove particles located in the very far beam distribution tails. Additionally, an also water-cooled variable aperture collimator is being installed in the last drift to the target to ensure no losses occur in the target vacuum chamber (TVC).

2.1.7. Failure scenarios

- Assessment of beam line component failures and their implications. Excessive beam losses on accelerator components can significantly impact operational reliability and functionality, distinct from distributed operational losses. Any failures, such as control, human error, cooling, loss of cryo, power outage, ... are manifested by the failure or degraded performance of the active elements in the beam line. Using the code TraceWin, we evaluated failures of all active beam line elements, i.e. solenoids, dipoles, quadrupoles, multipoles, and cavities, on the DONES linac, with a focus on energy deposition, loss distribution, and in the case of dipoles the direction of the lost beam at different field levels during the decay of the dipole field. A functional Machine Protection System (MPS) is crucial to halt the beam within microseconds of detecting anomalies. The study explored worst-case scenarios without an effective MPS and looked at the loss value in units of μJ μs^{-1}. Such a unit would be helpful in setting the response time of the MPS following an energy deposition analysis. Not all particle energy deposited in accelerator components directly causes damage; secondary particles carry away a portion of energy. While for machine protection, rapid localized losses are critical, the time-averaged amplitude is important for radiation

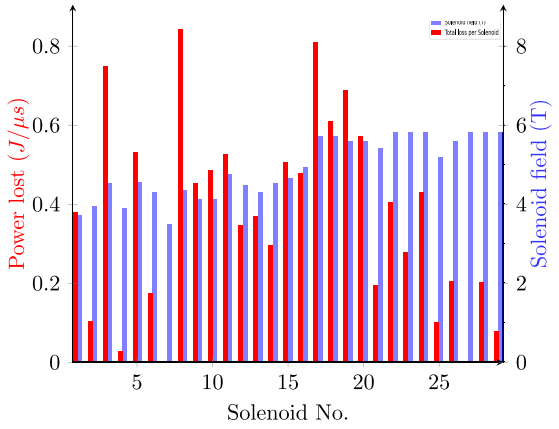

Figure 6. Integrated losses along the LINAC and the transferline due to failure of each solenoid and the nominal field of the solenoid which is failed.

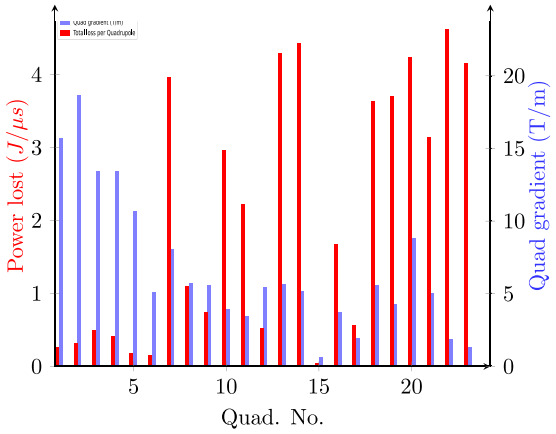

Figure 7. Integrated losses along the linac and the transferline due to failure of each quadrupole and the nominal gradient of the quadrupole which is failed.

safety, and hence in the dipole case, which has a very long decay time with respect to the MPS' reaction time, the direction of the loss was the figure of merit.

- Simulation details and results. The simulation of the failures is using 1×10^5 macro particles from a distribution (V16) which has been stored at the exit of RFQ, with an energy of $\approx$5 MeV and a beam current of $\approx$125 mA. The nominal end-to-end lattice of DONES in TraceWin code is used, with several elements such as the cavities and solenoids represented by fieldmaps. The study focused on understanding single-component failures without considering other errors.
- Failure impact analysis. Solenoids: figure 6 illustrates the downstream losses resulting from solenoid failures. The impact of solenoid field variations on total losses is shown, highlighting the critical role of phase advance in loss distribution. Quadrupoles: figure 7 depicts the downstream losses caused by quadrupole failures, similarly to the solenoids one can see that the lattice design, or the phase advance, has a bigger impact on the loss from a single focusing element than the strength of the failed component. The maximum integrated loss due to a failed quadrupole is approximately 4 J μs^{-1}, necessitating rapid response times of 5–10 μs for effective MPS operation. Multipoles: figure 8 shows the downstream loss distribution from multipole failures, indicating localized losses near the target. The maximum integrated loss for a failed multipole is minimal, this was an expected outcome as these elements are mainly shaping the beam distribution on the target. Cavities: the simulations consider varying levels of cavity field decay, affecting beam energy gain and focusing. Figure 9 presents the impact of cavity failures on downstream losses, when the field has totally decayed but the beam loading is not yet decelerating the beam. The maximum integrated loss for a failed cavity reaches approximately 1.6 J μs^{-1}, less than that of the quadrupoles, making protection against quadrupole failure the most demanding.

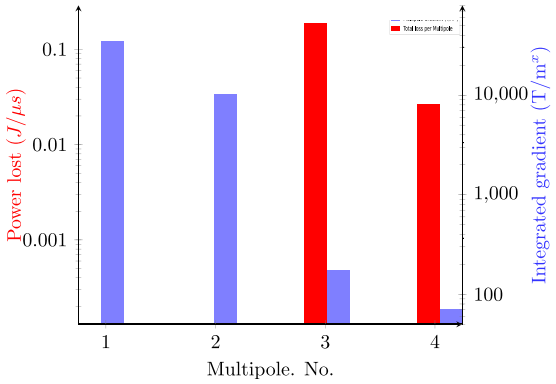

Figure 8. Integrated losses along the transferline due to failure of each multipole and the nominal gradient failed element.

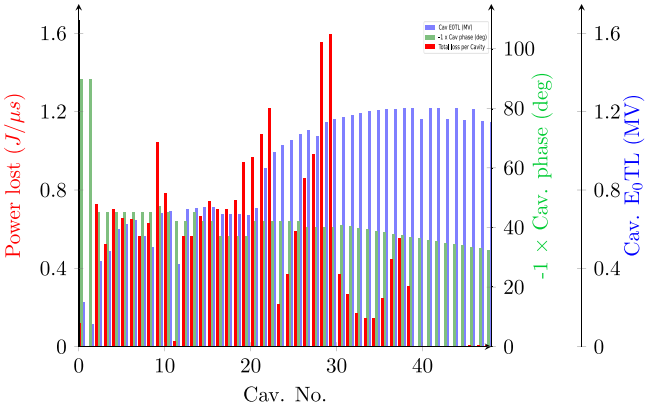

Figure 9. Integrated losses along the linac and the transferline due to failure of a cavity (at -100%) and the nominal voltage and phase of the failed cavity.

2.1.8. Optimization strategies. The required irradiation conditions of high energy deuteron beam are accomplished by shaping the beam profile by using non-linear magnetic

fields at the interaction point with the lithium jet. The irradiation requirements pertain to trade-off between the maximum beam power delivered by the accelerator driver, and the needs of neutron flux and minimum volume of irradiated materials. Note that there are uncertainties in a set of input parameters having impact in the output of interest pertaining in the simulations of neutron flux within TC. The uncertainties in the input parameter set can be handled using the stochastic approach, i.e. through the implementation of some stochastic approaches [29]. It is worth noting that traditional and the most commonly used methods are based on statistical approaches such as Monte Carlo (MC) simulations and various sampling techniques, being easy to implement but with the huge sample sizes, and also exhibiting rather slow convergence rate. Contrary to statistical approaches, the nonstatistical based techniques represent the unknown stochastic solution as a function of random input variables featuring an intrusive and non-intrusive approach, respectively. The intrusive methods imply more demanding implementation requiring a development of new codes, while the non-intrusive methods provide the use of a reliable deterministic model as a black box in stochastic computations. Generally, both intrusive and non-intrusive approaches exhibit fast convergence and high accuracy under different conditions. Recently, non-intrusive Stochastic Collocation (SC) method for uncertainty propagation (UP), uncertainty quantification (UQ) and sensitivity analysis (SA) has been implemented in static and dynamic simulations of neutron flux within TC [30]. SC can be regarded as a non-intrusive method applied to carry out UP and UQ. The advantage of SC vs MC is lower computational cost accomplished within the spectral approach framework. The successful implementation of SC method is illustrated on UP, UQ and SA of horizontal and vertical RMS beam sizes at the beam dump entrance [30]. Three quadrupoles of the last triplet of the BDTL are regarded as random variables, each represented by the uniform distribution as probability density function (pdf). Single deterministic simulation has been based on Tracewin calculations for the evolution of the beam along the BDTL. Additional example of UQ via SC method is carried out in case of RFQ transmission. Namely, magnetic fields of LEBT solenoids are modeled as RV. The outputs of interest are RFQ input current, RFQ output current and RFQ transmission. Thus, two stochastic problems are tested, one three-dimensional and the other two-dimensional. In both case studies, uncertainty of input parameters is propagated to the outputs of interest providing the computation of mean, variance, Kurtosis and skewness. Using the mean and variance, the confidence intervals for outputs are also calculated. SC is validated via MC with appreciably larger sample size. Furthermore, SA is carried out to rank input parameters from the most to the least significant regarding their impact on the output variance. Note that SA is performed by means of via one-at-a-time (OAT) and analysis-of-variance (ANOVA) approaches, thus using both local and global SA approach, respectively.

2.1.9. Start-to-end design. During the first year of the project, beam dynamics design and optimizations have been carried out separately for the different subsystems of the IFMIF-DONES accelerator. The input beam utilized for each subsystem is derived from the output beam of the preceding subsystem whenever relevant. With the completion of the design and analysis of each individual subsystem, the next crucial step involves simulating particle transportation from the start to the end of the accelerator. This simulation serves a dual purpose. Firstly, it ensures the coherence of the entire acceleration system and allows for the characterization of beam losses in the ideal case where no errors are considered. Then, error studies [31] for the entire accelerator will be based on the S2E model and will offer the opportunity to observe the cumulative effects of errors from one subsystem to the next. Start to end simulation results The beam density in the horizontal plane (x) and the vertical plane (y) is represented in figure 4. The position $z = 0$ is where the simulation starts, 189 mm after the ion source plasma electrode. The end of the beam line corresponds to the interface point between the deuteron beam and the lithium jet of the neutron production target. The black lines on this figure represent the beam pipes, which are entered in the simulation according to the design value. A precise definition of the beam pipe in the model is crucial, as any simulated particle exceeding this limit is regarded as lost. The MEBT scrapers are visible around $z = 12.2$ m, while the HEBT scrapers are located approximately at $z = 65.1$ m.

The beam losses along the DONES accelerator for the nominal case are represented in figure 10. Losses occur in the RFQ and in the first part of the MEBT (where the two scrapers are located), mainly at energies much less than 5 MeV. The power lost amounts several tens of watts locally, with a peak of 12 W just before the RFQ accelerating section, where the particles that are not correctly bunched are lost. Then, some losses are also observed on the scraper of the HEBT. Those scrapers are dedicated to eliminate beam halo, which would degrade the shape of the beam on the lithium target. Overall, in the MEBT, SRF LINAC, and HEBT, under the ideal assumption of no errors along the accelerator, no beam losses are observed, except in the components specifically designed for this purpose (scrapers).

Error study principle. To validate the design of the DONES accelerator, it is essential to assess the impact of errors on each component of the machine. For example, the alignment of accelerator elements will be performed within specified tolerance ranges. Furthermore, the power supplies will feed the various optical elements (solenoids, quadrupoles, dipoles, multipoles) or cavities (rebunchers or HWR) with a certain resolution and ripple. Conducting error studies enables determination of necessary tolerances and evaluation of their effects on the beam that can cause subsequent beam losses. Two main kinds of errors are considered are: static errors, and dynamic errors.

Static errors represent the possible misalignment of every elements of the accelerator. Typically, the order of magnitude

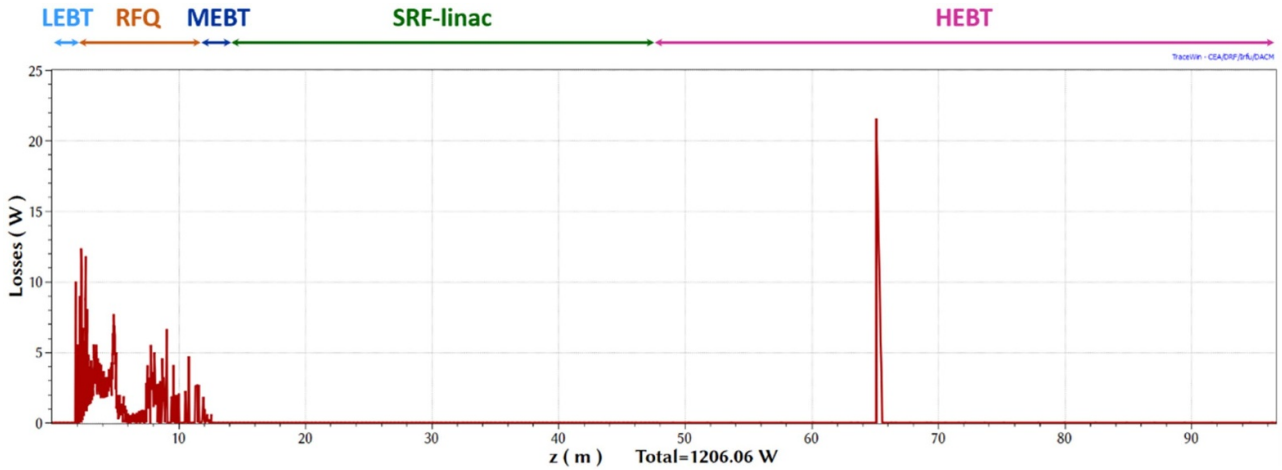

Figure 10. Beam losses along the IFMIF-DONES accelerator.

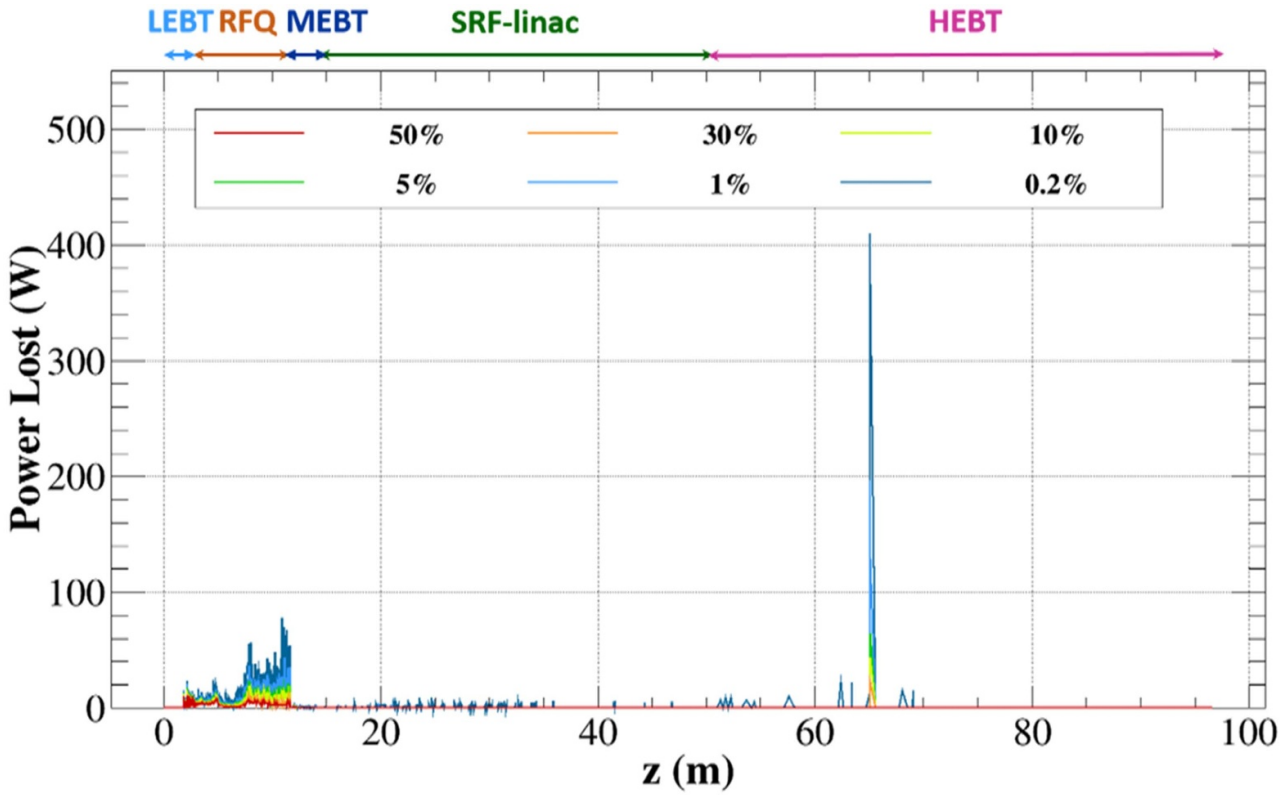

Figure 11. Beam power loss probabilities in the IFMIF-DONES accelerator (statistics over 500 accelerators with errors).

of the error considered, in accordance with alignment team, is around ± 0.1 mm for component at room temperature and around ± 1 mm for component that are inside the cryomodule. Off-axis beam excursions induced by these errors can limited by using an appropriate correction scheme. It relies on steering coils (H and V) associated with downstream beam position monitors (BPMs) (H and V). Each steering coil adjusts the beam center (the first-order moment of the beam distribution) to align with 0 (on the accelerator axis) at the position of the subsequent BPM. Dynamic errors represent imperfections such as vibrations or fluctuations or ripple in applied field or phase of the focusing/accelerating elements. These phenomena induce high-frequency perturbations on the beam for which no correction scheme is currently applied. A Monte-Carlo simulation method has been carried out by tracking 105 particles through 500 different accelerator, each of them having a different set of random static errors. The beam power loss probabilities along the DONES accelerator are shown in figure 11. Compared to the ideal machine without any error, the loss locations are similar: they occur mainly within the RFQ and on the HEBT scrapers. In rare cases (0.2%) losses can be observed in the SRF LINAC but remain below

Table 4. Outgassing rates q_{out} for hydrogen used in simulations.

	q_{out} (mbar l s^{-1} cm^{-2})
AISI 316L	9×10^{-11}
Aluminum	9×10^{-12}
OFHC Copper	9×10^{-12}
Electroplated copper	6×10^{-10}

1 W m^{-1}. Overall, in 90% of the cases in this error study, the losses are broadly comparable to those of the ideal case. In a next step, the dynamics errors will be included to the error study to further assess the robustness of the IFMIF-DONES accelerator design.

2.2. Vacuum

The vacuum subsystem of the IFMIF-DONES linear accelerator is designed to maintain optimal conditions for beam transport. Understanding gas sources is crucial for assessing their impact on pressure profiles and ensuring system performance. Key sources include beam neutral flow, thermal outgassing, beam losses, and injected gases. Accurate modeling using TPMC simulations, particularly with Molflow+, provides essential insights into gas behavior, deposition rates, and vacuum stability, informing design and operational strategies. Recent studies have been conducted to describe the subsystem in depth [32].

2.2.1. Gas sources. There are five different gas sources that can be found in the internal vacuum of the accelerator beam line. All these gas sources have been used as the boundary condition of vacuum modeling: (1) beam neutral flow, (2) thermal outgassing, (3) beam losses, (4) argon Injection, (5) krypton Injection, and (6) metal evaporation. The beam neutral flow has been calculated assuming an injection of a certain quantity of gas of D_2 for the beam. This is a conservative value that has been taken from knowledge of LIPAc, at 162 mA 3.9 sccm was reached in 2022. Subtracting from this value the beam losses and the required particle flow to get to a 162 mA beam, the beam neutral flow has been estimated as 1.97 sccm, or 3.3×10^{-2} mbar l s^{-1}. The gas composition within the beamline vacuum systems, when not in operation, primarily consists of gases thermally desorbed from internal surfaces what include all the chambers and beam instrument (main source of outgassing). It is expected that the residual gas after the commissioning period for vacuum (100 A h) will be composed mostly by water (<50), 30% hydrogen, 10% carbon monoxide, 4% carbon dioxide, and 1% argon. The outgassing rates of these materials depend on their composition, conditioning, and production history, potentially varying by several magnitudes. The thermal outgassing values from pre-baked stainless steel, aluminum, OFHC copper, and galvanized copper, can be seen in table 4. Niobium surfaces, presumed to be nearly saturated with a monolayer of hydrogen at 4.5 K, contribute negligibly to outgassing.

Table 5. Total and specific desorption rates for hydrogen isotopologue from the liquid lithium surface [18]. q is the specific outgassing rate, and Q the total desorption rate in two different units.

	Q		q
Species	(g h^{-1})	(mbar l s^{-1})	(mbar l s^{-1} cm^{-2})
H_2	4×10^{-8}	2.63×10^{-7}	2.83×10^{-10}
HD	3×10^{-9}	1.31×10^{-8}	1.41×10^{-11}
HT	2×10^{-9}	6.65×10^{-9}	7.05×10^{-12}
D_2	8×10^{-9}	2.63×10^{-8}	2.83×10^{-11}
T_2	1.2×10^{-8}	2.63×10^{-8}	2.83×10^{-11}

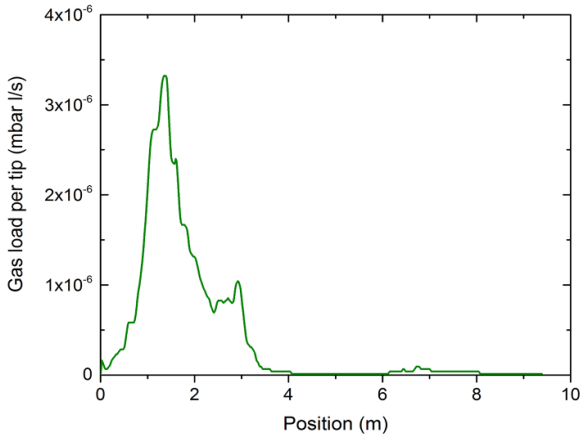

Figure 12. Gas load per tip along the position inside the RFQ caused by beam losses.

Additionally, the heated lithium surface contributes to thermal outgassing. Although the outgassing values for lithium are generally lower than those for other materials (see table 5), they are still considered. Beam losses are estimated based on the assumption that deuterium ions fully recombine into molecules upon reaching the surface. In the LEBT section, these losses are presumed to be evenly spread along the injection cone before the RFQ section. Within the RFQ, beam losses per tip follow a distribution that has been calculated through simulations (figure 12).

For the MEBT, SRF LINAC, HEBT, and Target sections, beam losses are assumed to be uniformly distributed at a rate of 1 W m^{-1} along the beamline tube. Some beam losses (and correspondent gas source) are expected: 30 W at the first MEBT scrapers, 1.1 kW at the HEBT scrapers and 1.6 kW at the HEBT collimator, and they are taken in account for the simulations. During normal operations, the lithium target is heated to around 570 K. To prevent boiling or significant vapor pressure of lithium, argon is introduced, maintaining the total pressure in the target chamber (TCV) between 1×10^{-5} and 1×10^{-4} mbar. Recent simulations for argon injection during standard beam operations at the lithium target have suggested an optimal gas injection rate of 7.1×10^{-3} mbar l s^{-1}, ensuring an argon partial pressure of approximately 1×10^{-4} mbar in the TCV. Krypton is planned to be used as a space charge compensation gas in the ECR source. The injection rate of Krypton from the ion source is 8.4×10^{-3} mbar l s^{-1}. Vapors

Table 6. Gas loads in mbar l s^{-1} the different subsections of IFMIF-DONES: Q_i from the deuteron gas neutral flow injected in the ion source, Q_{TH} from the thermal outgassing, Q_t from the deuteron gas flow (neutral gas or beam losses), Q_{Ar} from argon injection, Q_{Kr} from Krypton injection and Q_m from metal evaporation.

(mbar l s^{-1})	Q_i	Q_{TH}	Q_t	Q_{Ar}	Q_{Kr}	Q_m
LEBT	3.3×10^{-2}	1.8×10^{-6}	7.8×10^{-3}	7.1×10^{-3}	8.4×10^{-3}	—
RFQ	—	1.7×10^{-5}	1.2×10^{-3}	—	—	—
MEBT	—	1.1×10^{-5}	8.1×10^{-7}	—	—	—
SRF	—	8.3×10^{-6}	3.1×10^{-5}	—	—	—
HEBT	—	4.0×10^{-5}	8.7×10^{-6}	—	—	—
LT	—	2.0×10^{-6}	3.3×10^{-8}[a]	—	—	(Li) 65 (K) 86 (Na) 19

[a] Desorption of D_2 and HT from the liquid lithium surface at target.

of lithium, potassium, and sodium from the TCV may enter the beamline, where they condense on its cooler components. The deposition rates for various sections of the beamline near the target have been calculated, assuming a period of operation time of 340 days.

Table 6 summarizes the gas loads by thermal outgassing, beam losses, argon injection at target and krypton injection in the ECR and metal evaporation at the liquid lithium surface.

2.2.2. Modeling. Multiple investigations have been conducted to provide an initial estimation of the pressure profiles within the linear accelerator of IFMIF-DONES [33]. The primary computational tool utilized for these analyses is the direct test-particle MC (TPMC) method, specifically the Molflow+ software [34] developed by CERN Additionally, studies have incorporated findings from the prototype accelerator LIPAc, given that its initial section corresponds to that of IFMIF-DONES. The scope of these studies encompasses the following areas: (1) analysis of metal re-sublimation affecting beamline components, (2) determination of monolayer formation time within the cryomodules, (3) evaluation of effective pumping speeds in the cryomodules and (4) comprehensive simulation of the linear accelerator. The study on metal re-sublimation focused on estimating the deposition rates of metallic layers on beamline components near the target over an operational period of one year. To achieve this, distinct models were employed for lithium, potassium, and sodium. The resulting metal layer thicknesses exhibit significant spatial variation, as demonstrated in figure 13. Gaps observed in the distribution diagrams correspond to regions within the model that were not impacted, primarily due to shadowing effects. The thickness of deposited layers decreases markedly with increasing distance from the target, though lithium accumulation near the target chamber can reach several millimeters within one year. The presence of peaks in deposition thickness is attributed to localized reductions in cross-sectional areas. Despite these accumulations, the vacuum performance is expected to remain stable, provided that the deposited layers do not substantially elevate the overall outgassing rate.

To ensure compliance with reliability and cleanliness requirements, the monolayer formation time in the first and last cryomodules was computed. The time required for the

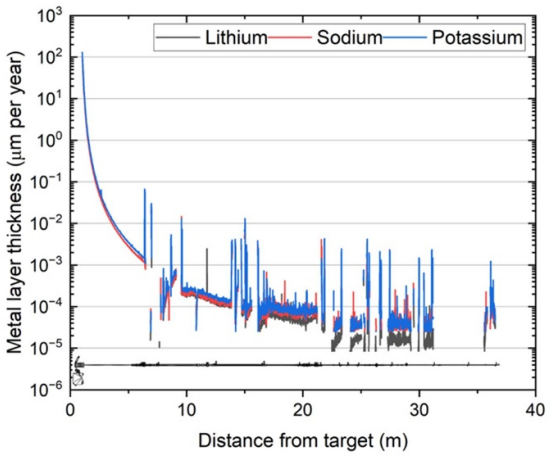

Figure 13. Metal layer thickness of lithium, sodium and potassium after one year of operation.

formation of a complete monolayer in the initial and final cavities was determined to be 423 days and 278 days, respectively. To mitigate excessive adsorption, the final cavity must undergo thermal cycling every three years, thereby preventing the accumulation of more than four monolayers. The effective pumping speed of the cryomodule was determined through a submodel that integrates the HEBT system and the linking tube between the final cavity of the SRF-Linac and the HEBT. The calculated effective pumping speed at the exit of the last cavity was 8.5 l s^{-1}, based on nitrogen gas at a temperature of 293 K. A full-scale simulation of the accelerator was performed using TPMC methods to analyze particles with molar masses of 4 (primarily originating from beam losses), 2, 28, and 44 (arising from thermal outgassing), 40 (introduced through argon injection and thermal outgassing), and 84 (resulting from krypton injection at the electron cyclotron resonance (ECR) source). Partial pressures were quantified by tracking particle interactions with designated surfaces along the beam axis, enabling the computation of total pressure through the summation of these individual contributions. The distribution of gas pressure within the IFMIF-DONES accelerator is illustrated in figure 14, while figure 15 presents the pressure values normalized to a temperature of 293 K. The pressure distribution elucidates the spatial variation of gas loads induced by beam

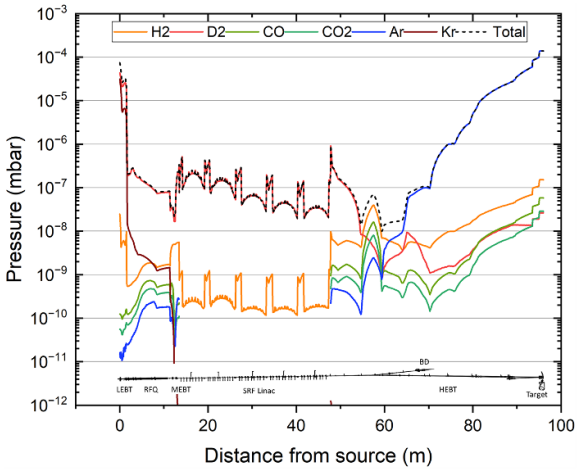

Figure 14. Gas pressure profile for deuterium (mainly beam losses), hydrogen, carbon monoxide, carbon dioxide (thermal outgassing), argon and krypton injection and total pressure in the IFMIF-DONES accelerator at beam operation (beam goes to target). Reprinted from [32], Copyright (2025), with permission from Elsevier.

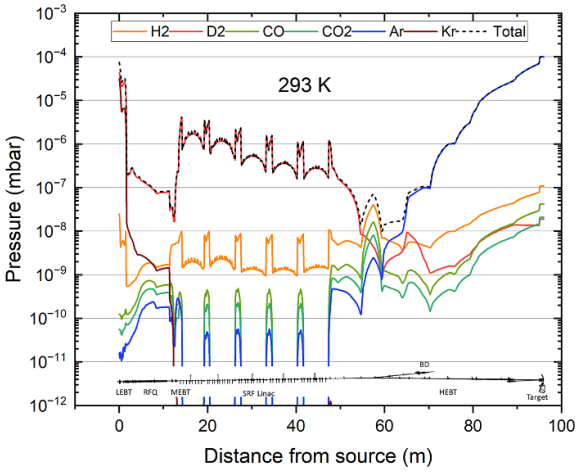

Figure 15. Gas pressure profile for deuterium (mainly beam losses), hydrogen, carbon monoxide, carbon dioxide (thermal outgassing), argon and krypton injection and total pressure in the IFMIF-DONES accelerator at beam operation (beam goes to target). All pressures are normalized to 293 K.

losses in the LEBT, RFQ, Medium-Energy Beam Transport (MEBT), and SRF-Linac sections. Furthermore, the pressure levels in proximity to the target within the HEBT region are significantly influenced by the injected argon. Notable pressure peaks between LINAC modules are primarily attributed to localized temperature variations and the associated increase in outgassing rates.

2.2.3. Engineering design. The vacuum system of the linear accelerator of IFMIF-DONES has been divided into sections corresponding to those of the accelerator itself. Two of these sections are further divided into subsections. The sections of the vacuum system are as follows: (1) Injector or LEBT, (2) RFQ, (3) MEBT, (4) SRF LINAC) (5) One subsection per each cryomodule (five in total), (6) HEBT, splitted in section 1, dipole junction, beam dump section, section 2, section 3 and radiation isolation room (RIR)/target interface room (TIR) to target.

The vacuum requirement of the LEBT and RFQ is to maintain a pressure lower than 5×10^{-7} mbar, while the requirement for the remaining sections is to be lower than 5×10^{-8} mbar. Also, the SRF LINAc and its neighboring sections (at least 5 m) must be particle-free to avoid field emission on the surface of SRF cavity due to the high electric fields, minimize surface resistance since particles can disrupt the superconducting state and consequently degrade the quality factor (Q_0), and prevent thermal instabilities caused by localized heating when exposed to RF fields. It is also possible for particles to be transported by the electrical and magnetic fields associated with a charged beam. To meet these requirements, only turbomolecular pumps (TMPs) and non-evaporable getter (NEG) pumps are used as high vacuum pumps. In every section, there are vacuum stations where at least two TMPs are connected to the beam cavity. The outlet of these TMPs is connected to two backing pumps in parallel. These backing pumps are dry multi-stage roots pumps. They are in an adjacent room to ease maintenance. The NEG pumps are used near the SRF LINAC, where the pressure requirement and particle free requirements are more restrictive. Each vacuum station is equipped with Pirani and Penning gauges to monitor the pressure continuously, as well as throughout the beam chamber. Residual Gas Analyzers (RGAs) area is also used in each section to better control the gas composition of the beamline. The injector vacuum consists of two vacuum stations, each with only one TMP. It is a special case as the gas load near the source is quite high. The RFQ vacuum section consists of two groups of TMPs each, one at each side. They are distributed asymmetrically to be able to pump the expected high beam loss at the beginning of the section. The MEBT vacuum section comprises a vacuum station of three TMPs and a NEG pump, it also allows a connection to a slow pumping system (SPS) for its initial pump-down. The SPS is a vacuum station mounted in a trolley; however, the inlet of its TMP can be regulated through a mass flow controller (MFC), ensuring a laminar regime during the pump-down. The SRF LINAc vacuum is divided into three different locations: the beamline, the insulation and the warm sections. First, the beamline vacuum of each cryomodule is done by using the SPS, only one pump down is needed before cooling them down. Then, the insulation vacuum is achieved by one TMP in each of the cryomodules, and each warm section has a NEG pump, and if there is enough space a TMP. Finally, the HEBT section consists of five sections each pumped by groups of four turbopumps each, with the exception of the Dipole junction that only has two. The closest vacuum station of the first section of the HEBT is pumped down by an SPS to ensure that it is particle free. Additionally, an Argon Cold Trap is expected in the dipole junction section of HEBT to reduce the gas load of Ar and significantly increase the monolayer formation time in the SRF LINAc.

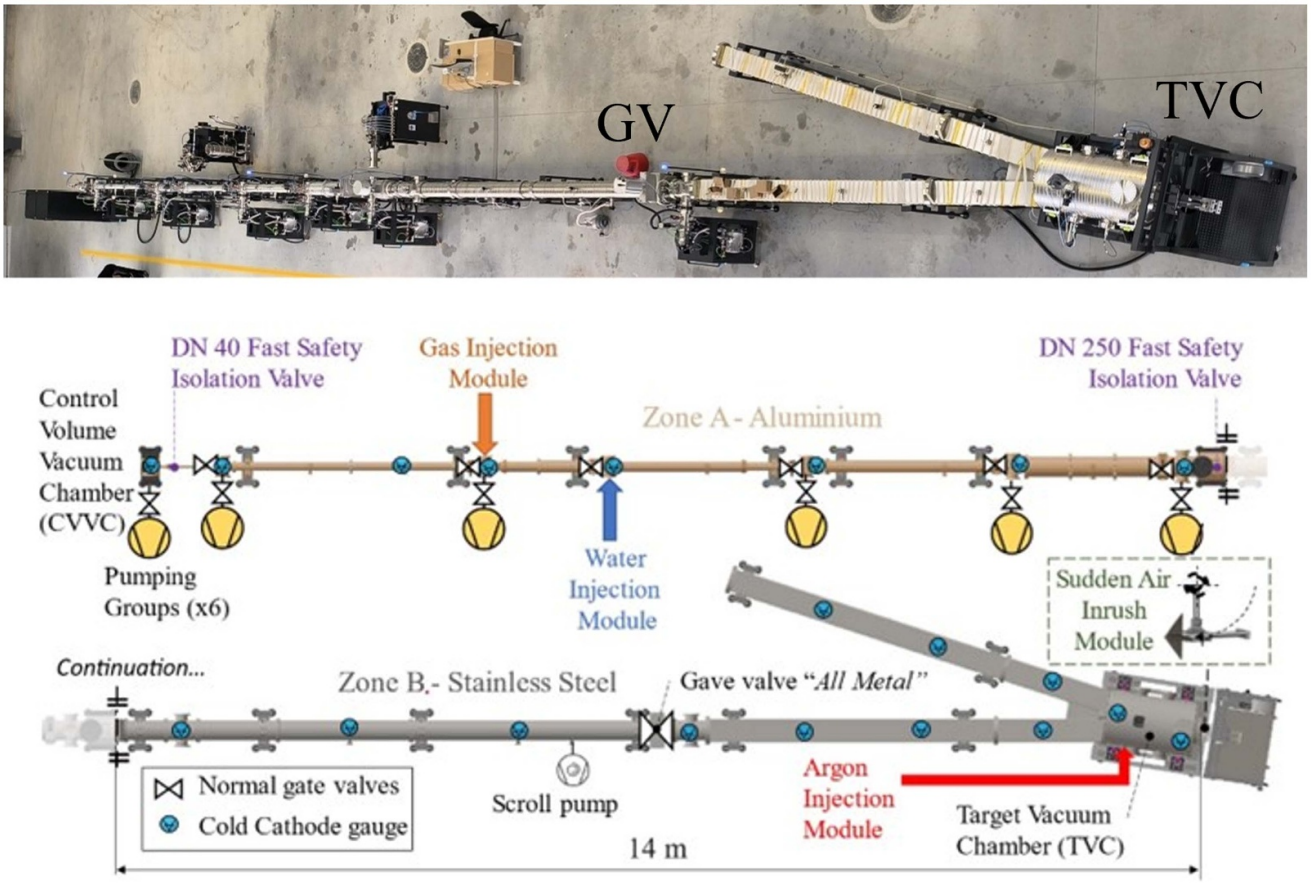

Figure 16. Picture (top) and sketch (bottom) of the MuVacAS facility.

2.2.4. Accidental scenarios. One of the particularities of the IFMIF-DONES accelerator is the lack of separation window between the TVC and the rest of the accelerator vacuum line. This is due to the high power and low energy of the beam, which would imply a huge power deposition in such a thin window, with no material that could withstand this load and no means of cooling it. This particularity has some safety implications since in loss of vacuum accidents (LOVAs) [35], the entering air could reach the liquid lithium of the target or activated material from it could be transported through the accelerator line. To mitigate this, we rely on Fast Safety Isolation Valves (FSIVs) which, when closing, can isolate the TVC in 100 ms in case a LOVA is detected, acting as a safety confinement barrier. The MuVacAS (Multipurpose Vacuum Accident Scenarios) is an experimental setup (figure 16) installed in an auxiliary building at the DONES site to study these LOVAs due to leaks or abrupt inrushes to validate the FSIVs and assist their Safety Qualification in views of the licensing of IFMIF-DONES.

In addition, MuVacAS is serving as a laboratory to test and validate relevant vacuum components that will be installed in the IFMIF-DONES LINAC, such as pumping system, measurement systems, aluminum chambers, flanges MKS ISO, differential pressure system, the control systems, and integration of remote handling (RH) Quick Disconnection Systems (QDS) to evaluate the connection between the TIR and TVC-HEBT elements.

For this purpose, MuVacAS reproduces as close as possible the characteristics and specifications of the vacuum chambers of the IFMIF-DONES HEBT+TVC as illustrated in figure 16. It also includes three experimental modules to recreate the identified scenarios as the injection of gas (N_2, Ar, air, He) or water demineralized, and the recreation of sudden air inrush; and fast acquisition system (20 kHz) to record and characterize these events, and the effectiveness of the mitigation measures.

The vacuum system of MuVacAS consists of three main zones (figure 16) The Control Volume Vacuum Chamber (CVVC), which allows a precise measurement of the amount of incoming gas at the extremity of the target chamber during the vacuum loss experiments. The vacuum line, which represents the HEBT geometry in terms of its duct diameters according to the most updated HEBT design. Most of the fixed flanges used are ISO CF flanges with diameters ranging from DN40 to DN250. And the TVC, where the main geometrical characteristics are taken from the design of the TVC IFMIF-DONES, which look-like a cylinder with a diameter of 600 mm, and a length of 1135 mm.

The total length of MuVacAS is 28 m due to space limitations, compared to the 49 m of the IFMIF-DONES HEBT+TVC chambers. The setup is composed of two main

zones (A, B) as shown in (figure 16). Zone A is scaled down with respect to IFMIF-DONES (14 m vs 35 m). Zone B, on the other hand, retains a longitudinal and transversal scale of 1:1 (14 m), from the TVC to the last meters of the HEBT (downstream of the FIV DN250), which is the region of greatest interest in the accident scenarios. In terms of materials, zone A is made of aluminum, and zone B of stainless steel AISI 316L, consistently with the current HEBT design. The TVC, however, is made of 304L Stainless Steel with a wall thickness of 1 cm. This is to evaluate its eventual implementation in the final HEBT design.

There are six pumping groups (PGs) distributed along the vacuum line as shown in (figure 16). If required, they can be reconfigured to a different location on the vacuum line. Each PG can be isolated when performing the test. The vacuum line has seven gate valves (GV1–GV7) along the line.

The differential pressure system contains an argon injection module composed of one MFC with a range of 1×10^{-4} sccm–1 sccm, one remote-controlled valve, with connections to be fully compatible with the high vacuum line, and one external controller. The injection can be controlled by a closed loop, considering the pressures of the TVC to keep them within their limits of 1×10^{-4} mbar–1×10^{-5} mbar.

The MuVacAS control houses the I/O PC (DELL), the I/O controller based on PLC (redundant system with two CPUs), the safety system (PILZ), the fast gate valve controller, two cDAQ for the fast instrumentation, the TPG 500 controller to acquire the signals of the pressure gauges. The system has three protocols used for communication: EPICS protocols with process variables (PV), the protocol of PLC, and the protocol TSN (based on a protocol IEEE802.1) for the fast acquisition data.

2.3. Accelerator control and operation

Every system of the accelerator (section 3) provides its controls as part of a more complex control architecture of the facility, which involves low-level control and high-level orchestration. The entire control system architecture realizes a two-layer structure where the lower layer contains both the field device interface and low-level control logic. In contrast, the upper layer handles high-level control, control services, and the Human-Machine Interfaces. The last version of the EPICS framework, EPICS 7 [36], provides the interface between these layers. EPICS 7 introduces several new features and improvements compared to the well-known EPICS V3, including support for structured data, improved network protocols, and better performance and scalability. In addition, due to the characteristic of integration of heterogeneous kinds of hardware, software, and protocols, EPICS is used to implement a part of the controls related to different functional subsystems (radio frequency, vacuum, cooling, etc), providing a common middle layer which standardizes the communication among the various hardware and software solutions.

Different systems need different characteristics in terms of requirements. Therefore, various technologies must be used in different contexts: industrial technologies such as PLC-based solutions are chosen for tasks where security is the most critical feature. PLCs provide reliable and robust control in environments where safety is paramount. In scenarios where the acquisition speed rate is crucial, a fast acquisition system based on the Versa Module Eurocard (VME) bus can be a good candidate. However, due to its age, the VME system shall be migrated to a newer solution. Currently, micro telecommunications computing architecture (μTCA) is under investigation as a potential replacement, offering faster processing speeds, higher reliability, and better support for modern applications. Common hardware (such as embedded systems) is chosen when only integration is required. These systems provide flexibility and ease of integration without the need for specialized hardware. Additionally, all the technologies used in the LIPAc project require upgrading and migration to newer solutions. This includes a comprehensive evaluation of current technologies and the identification of suitable modern alternatives. Several studies are underway to identify good candidates for these upgrades, focusing on improving performance and compatibility. A significant effort in standardizing the architecture, devices, hardware, software tools, and applications has been performed to ensure seamless integration and interoperability across the entire system. The standardization work is crucial in the early stages and the developing of unified guidelines and protocols for device communication and data exchange, the selection of standardized hardware platforms and interfaces to simplify maintenance and upgrades, the implementation of consistent software tools and development environments to streamline application development and deployment, and ensuring that all components conform to the same set of standards to reduce complexity and improve system reliability. Preliminary indications and guidelines for this standardization process are already being formulated, laying the groundwork for a more cohesive and efficient control system architecture. Furthermore, the adoption of EPICS seven opens possibilities for integrating machine learning technologies and solutions. The advanced data handling capabilities and improved performance of EPICS 7, in addition to the different APIs to the principal program languages (i.e. Python), facilitate the incorporation of machine learning algorithms, which can enhance system diagnostics, predictive maintenance, and overall operational efficiency. Preliminary studies on ML/AI are already ongoing by different partners in the DONES project, and the results can be used as guidelines for future requirements in the control architecture, to achieve smarter and more autonomous control systems, further advancing the capabilities of the project.

2.4. Accelerator commissioning

The accelerator will be commissioned in four main phases (see figure 17), which are similar to the ones in comparable accelerator facilities. During the first phase (*Phase 1*), the injector will be tested and characterized up to CW, and in the main modes of operation. This is a crucial stage for the success of the accelerator beam transport during the following stages, since the characterization of the beam at injector is limited. Besides the nominal operation of the 40 MeV deuteron beam, during the staged commissioning phases, the accelerator will be tested

with protons at scaled energy of 20 MeV, and peak beam current of 70 mA.

The second phase (*Phase 2*) corresponds to the commissioning of the RFQ together with the MEBT. A very careful and detailed characterization of the beam at this stage is mandatory in order to ensure a proper acceleration of the beam along the superconducting LINAC. For this reason, a Diagnostics Plate is installed at the output of the MEBT during this phase. The plate contains all the necessary diagnostics for the characterization of the main beam parameters. At this stage, the beam will be operated in pulse mode, but ramping up to a relevant duty cycle of up to 20%. This percentage is considered already relevant to validate the good behavior and the tuning of all the components. For this reason, a HPBD is required during this phase. In order to optimize the hardware, the beam dump used at the HEBT will be used during this phase, located downstream the RFQ.

Once *Phase 2* is completed, the diagnostics plate and the beam dump will be moved to the final location at the BDTL of the HEBT (section 3.5). The SRF LINAC will be installed downstream the MEBT, together with the HEBT. At first moment, the SRF LINAC will be characterized with a pulsed beam using the BDTL of the HEBT with a duty cycle up to 1% (50 kW).

The last stage before nominal operation (*Phase 4*) is the ramp up with the BOT. A pilot beam with very short pulses will be first used to tune critical parameters of this line: the profile at the multipole area, the transport down the target, and the position and profile at the target.

At least five years are allocated for the completion of the four phases before switching to normal experimental operation irradiating materials.

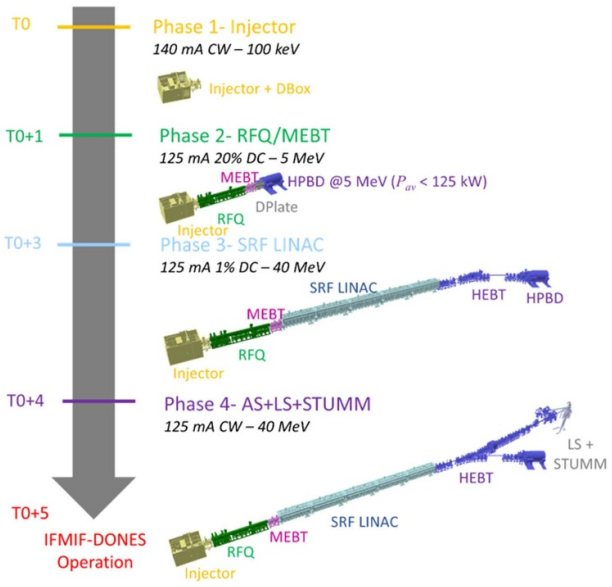

Figure 17. Commissioning phases of the IFMIF-DONES accelerator.

3. Systems design

The complexity of the engineering design of IFMIF-DONES is handled by the application of system engineering to the accelerator components. The functions of delivering a high-energy and current deuteron beam are accomplished by the ASs, which are formed by the following systems: (1) the injector (section 3.1) composed of the ion source and LEBT, (2) the RFQ (section 3.2), (3) the MEBT line (section 3.3), (4) the SRF LINAC (section 3.4), (5) the HEBT (section 3.5), (6) the RFPS (section 3.7) and (7) the ASs Ancillaries (ASA, section 3.8). For each of them, a bunch of system requirements and interfaces have been defined. In the following, the most important features of the design of each system will be developed.

3.1. Ion source and LEBT

The injector system (IS) aims at injecting in direct current (DC) operation a stable 100 keV–140 mA deuteron ion beam into the RFQ with small transverse emittances and low energy dispersion, and with D+ species fraction of 99% or more. This intensity at the level of the IS is defined considering both the beam intensity required at the lithium target location (125 mA) and the transmission through the whole accelerator (above 90%). An ECR ion source has been selected since it is recognized worldwide as the most efficient devices to reach such performances with high reliability—availability [37–41]. During commissioning phase, other modes of operation are requested: production of an equal perveance proton beam of half current and half energy as nominal with deuteron beam to avoid activation of the accelerator components due to beam losses, and pulsed operation mode either by only switching the magnetron of the ECR source or by inserting a chopper (in addition to the switch of the magnetron) in the LEBT line to produce beam pulses as short as 100 μs length and to decrease thus the average beam power. In order to match the beam at the entrance of the RFQ, appropriate characteristics in the transverse phase planes shall be met, that is defined by the normalized transverse (horizontal and vertical) emittances which shall remain below 0.30 π mm $\cdot$ mrad, and also by the Twiss parameters that can be varied in a certain range thanks to the tuning of the currents of the LEBT solenoids. The IS shall stop the beam production in less than 10 microseconds to avoid damage of the systems concerned. For that, a fast magnetron shutdown system (FMSS) is implemented. In order to ensure the required inherent availability of the whole AS of 87% over the whole lifetime of the project (30 yr) [42], the injector shall be designed to fulfill the RAMI requirements with an inherent availability higher than 87%. Table 7 shows the main parameters that are required for the DONES IS.

The IS (figure 18) is made of three subsystems. First, the ECR source and the accelerator column composed of five electrodes allow the creation, extraction and acceleration of deuteron ions in order to generate a high intensity DC deuteron beam at 100 keV. Then, the LEBT line aims at guiding and matching the beam to the RFQ by means of two solenoids with integrated steerers. It also allows to chop the beam in the pulsed operation mode. Several beam diagnostics are installed

Table 7. Main parameters of the DONES Injector System where: I_{out} is the value of the extracted D^+ or H^+ current out of the LEBT,E_{out} is the output energy of D^+ or H^+ out of the LEBT, F_{D+} the fraction of D^+ current in the total current extracted, I_{out} (rms) the value of the jitter of the extracted current, $\epsilon_{out,norm}$ the value of the normalized emittance of the extracted current, *DC* the value of the duty cycle, $t_{b,off}$ the switch off time of the beam, t_{LT} the lifetime of the source, and IA the inherent availability.

Parameter	Value	Remarks
Ion type	D+	H+ (comm.)
I_{out} (mA)	140	70 (H+)
E_{out} (keV)	100	50 (H+)
F_{D+} (%)	99	out LEBT
I_{out} (rms)	1% rms	$\leqslant$1 MHz
$\epsilon_{out,norm}$ (π mm·mrad	$\leqslant$0.30	
Twiss	TBD	
DC (%)	100	Pulsed (comm.)
$t_{b,off}$ (μs)	$<$10	
t_{LT} (years)	30	
IA (%)	$<$87	

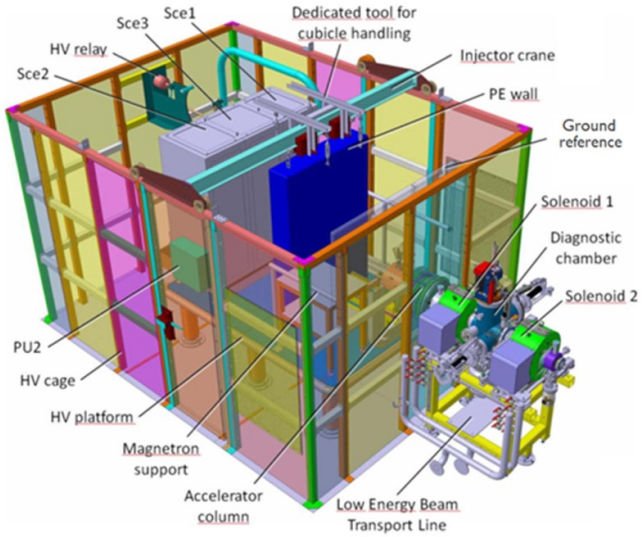

Figure 18. Mockup of the DONES Injector.

in the LEBT to characterize and control the beam. Finally, the local instrumentation and control subsystem (LICS) enables the tuning, monitoring and analysis of injector parameters during the conditioning and operation phases.

The Injector of LIPAc, prototype for DONES, was designed and constructed by CEA Paris-Saclay. Its ECR ion source is based on the SILHI source design [43]. It has been under commissioning since 2014 in Rokkasho, Japan. Using an electrode plasma with an opening of 11 mm diameter, requirements have been met since 137 mA of 100 keV D^+ beam could be extracted in a stable way during 11 h in DC operation. The normalized emittance was measured at low duty cycle and was of 0.24 pi mm.mrad, which is under specifications. The noise of the beam current was measured with the beam stopper and was of 2.6% rms, which is in the same level that the required value. Commissioning have been then pursued using an electrode plasma with an opening slightly higher (11.5 mm) for optimization and first results are promising [9]. Taking benefit from the experience gained with the LIPAc injector, components of this injector that are satisfactory are kept unchanged for DONES injector. Other components should need improvements and proposals have been given to fulfill the current requirements and interfaces of DONES. As a high priority, it has been identified for instance the design improvement of the accelerator column to ease the assembly, alignment procedure, and therefore final position accuracy of the electrodes, of the EMU to provide easier alignment of the slits and of the chopper to chop completely the beam outside the chopper gate. Several other improvements have been identified [44].

Table 8. Main RF parameters of the DONES RFQ. R_S is the Shunt Impedance, Q_0 the unloaded quality factor of the cavity, P_{dis} the dissipated power, E_{st} the stored energy, and $P_{RF,tot}$ the total RF Power. Q_0, P_{dis} and $P_{RF,tot}$ include a 20% margin for RF regulations and residual reflections.

R_S	206–270 kΩ
Q_0	12 800
P_{dis}	585 kW
E_{st}	6.6 J
$P_{RF,tot}$	1345 kW

3.2. RFQ

The IFMIF-DONES RFQ is a CW accelerating structure and one of the engineering challenges of the DONES design. Currently, a lot of research is ongoing within the accelerator field on RFQ as a driver of CW accelerators [45]. In case of the DONES RFQ, the structure must handle a power dissipation of more than 600 kW while keeping the activation due to beam losses as low as possible. The resonator of IFMIF-DONES RFQ (figure 19) is a 10 m length four-vane structure with and the necessary tuning of the cut off frequency due to R_0 and Voltage variation is obtained by varying the electrode thickness (inductive region tuning) along the structure [46]; in this way the shunt impedance is higher where the voltage is larger. The RFQ section is also optimized to reduce RF losses $Q_0 > 10000$. As the cavity is significantly longer than the wavelength, in order to guarantee a proper implementation of the voltage law (maximum deviation of $\pm$2% from the nominal one, due to contamination of the mode induced by geometrical errors) and the attainment of the operational frequency, the RF tuning of this long cavity is performed by a set of 108 tuners, to be machined to length after the assembly of the module according to the RF measurements and the implementation of a tuning algorithm [47]. The main RF parameters of the RFQ are listed in table 8.

The structure is made of copper (CuC_2) and is expected to be precisely machined in several modules that contain the couplers, tuners and vacuum ports which are later joined in a so-called supermodule using vacuum brazing. The complete structure is then combined with three supermodules.

The control of the frequency in the cavity is performed using the input temperature of the water cooling to the RFQ vanes. This method of operation was verified first with thermal

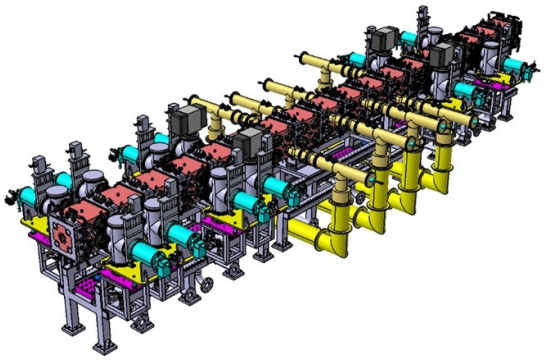

Figure 19. Mockup of the DONES RFQ.

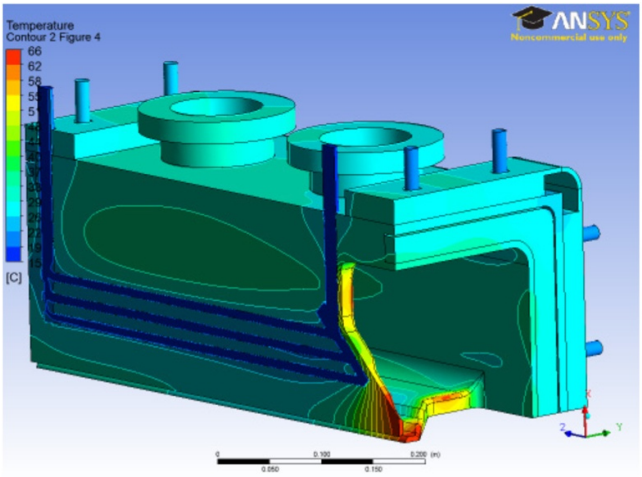

Figure 20. Temperature distribution in the vane undercuts with nominal RF power. The maximum value is equal to 66 °C.

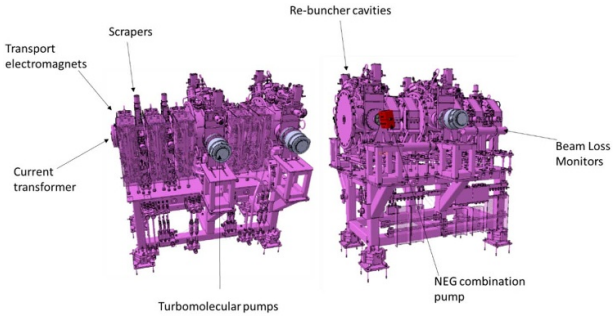

Figure 21. Mockup of the DONES MEBT.

simulations [48] and then recently experimentally during the Phase B+ of commissioning of the LIPAc RFQ full-scale prototype. Therefore, the RFQ cooling loop plays a crucial role in tuning the cavity and maintaining the desired voltage profile along the structure by precisely controlling the temperature within ±0.1 °C (see also in section 3.8.1). To achieve this, the RFQ features two distinct manifolds and cooling circuits—warm and cold—each equipped with three water inlets. In the design phase, The FEM analysis revealed that the turbulent flow was not uniform along the duct. Since temperature uniformity is essential for proper cavity operation, we opted for a smooth duct design on the vessel, despite the resulting reduction in the heat transfer coefficient. Consequently, in this way, the relative positioning of the cooling channels was designed. To account for temperature, rise, and variations in the convective coefficient along the module, we enhanced the integrated thermal-CFD analysis using Ansys CFX 12 and the thermal-structural analysis with Ansys Workbench 12. These improvements also ensure a consistent mass flow in the vane cooling ducts. A 3D detail about the undercut thermal design is reported in figure 20. From [49]. More details about the cooling design are reported in [50, 51].

The field level and field distribution in the cavity is monitored by pick-up loops distributed throughout the cavity. Some of these pickups also give the signal for actual power level to the LICS and LLRF. An additional voltage adjustment during operation is achieved by independently varying the vessel inlet water temperature in each of the three RFQ supermodules [52]. RF power is injected into the RFQ via eight independent loop power couplers, based on Alumina planar brazed RF windows. Each RF line is equipped with directional couplers for monitoring forward and reverse power at each line.

3.3. Medium-energy transport line

In the case of IFMIF-DONES, the very high space charge forces require a very short distance of the focusing elements to counteract them, as can be seen in figure 21. The MEBT is thus a very compact line. Five short quadrupole electromagnets with a maximum gradient of 25 T m^{-1} control the transverse beam dynamics. The same iron yoke has nested coils to create dipolar magnetic fields in the horizontal and vertical fields to steer the beam trajectory. Four BPMs, located in the middle of the electromagnets axis, provide the feedback to tune the beam position. In the longitudinal plane, two rebuncher cavities adapt the bunch time structure to the needs of the first superconducting cavity downstream. The cavities provide a maximum effective field of 350 kV, based on the use of an interdigital H (IH) cavity with five gaps created in-between four drift tubes. The cavity tanks are made of copper coated stainless steel, which contain water cooled channels. Screened vacuum ports are located at each buncher. In addition, a couple of beam scrapers, with four movable copper blades, help the purification of the beam particles with the wrong dynamics. Up to 500 W can be removed per each water cooled blade. An additional set of beam diagnostics monitor the line performance, such as current transformers to monitor the beam current at the interface with the RFQ, or beam loss monitors along the line. Main parameters of the MEBT are summarized in table 9.

3.4. Superconducting acceleration

The beam acceleration is provided by superconducting radio frequency (SRF) Half Wave Resonators (HWR) operating at a central frequency of 175 MHz and 4.45 K. This frequency can be adjusted with a mechanical frequency tuner which deforms

Table 9. Main MEBT parameters. L is the beam dynamics length, E_{nom} the nominal particle energy, $\epsilon_{\mathrm{in,norm}}$ the maximum beam emittance at the input interface, I_{in} the maximum average particle current at the input, DC the duty cycle, I_{in} the average particle current at the output, E_0LT the maximum effective voltage of the re-buncher cavities, $P_{\mathrm{c,max}}$ the maximum power of the couplers of the re-buncher cavities, $B_{\mathrm{quad,max}}$ the maximum magnetic field density of the quadrupole magnets, $Bl_{\mathrm{st,max}}$ the maximum integrated magnetic field of the correctors, p_{in} the pressure at the interface with the RFQ, p_{out} the pressure at the interface with the SRF LINAC.

L	2.35 m
E_{nom}	2.5 MeV u^{-1}
$\epsilon_{\mathrm{in,norm}}$	0.3 π mm · mrad
I_{in}	125 mA
DC	CW
I_{out}/I_{in}	>99.9%
E_0LT	350 kV
$P_{\mathrm{c,max}}$	15 kW
$B_{\mathrm{quad,max}}$	25 T m^{-1}
$Bl_{\mathrm{st,max}}$	25 G m
p_{in}	$<5\times10^{-7}$ hPa
p_{out}	$<5\times10^{-8}$ hPa

Table 10. Main parameters of the SRF LINAC components. E_{nom} is the nominal cavity acceleration field, Q_0 the cavity unloaded quality factor, f_{c} the resonance frequency of the cavity, T_{wc} the cavity cooling temperature, P_{tr} the transmitted RF power of the coupler, B_z the magnetic field at the axis of the solenoid, B_zl the integrated magnetic field along the axis, and T_{ws} the solenoid coolant temperature.

Component	Parameters	β_{low}–β_{high}
Cavity	E_{nom} (MV m^{-1})	4.5
	Q_0 @ E_acc_nom	5×10^8–1×10^9
	f_{c} (MHz)	∼175
	T_{wc} (K)	4.45
Power coupler	P_{tr} (kW)	100–200
Solenoid	B_z (T)	6
	$B_{\mathrm{s}}l$ (mT · m)	7
	T_{ws} (K)	4.45

the HWR to slightly shift their resonant frequency (−50 kHz). The beam is also focused with superconducting solenoids operating at 6 T and 4.45 K which are equipped with horizontal & vertical pairs of coils for beam steering and BPMs for beam monitoring. The accelerating electromagnetic wave is transmitted to the HWRs through the RF power couplers which were designed for a maximum continuous transmitted power of 200 kW. Main parameters of the SRF LINAC components are compiled in table 10.

As it can be seen in figure 22, the SRF LiNAC is split into five cryomodules (two low-β and three high-β), each linked by warm sections incorporating a pumping system associated to a gate valve and with the potential to add some beam diagnostics like SEM-grids for beam commissioning. The main parameters of the cryomodules are summarized in table 11.

The main components were designed based on the LIPAc cryomodule [53] which is currently being assembled for the

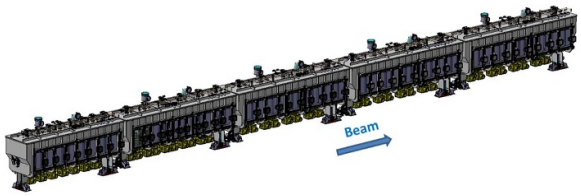

Figure 22. Mockup of the DONES SRF LINAC.

Table 11. SRF LINAC main parameters: CM is the cryomodule, β is the optimized deuteron speed at the cavities, Seq. the lattice sequence at each cryomodule, S are solenoids, C are cavities, N_{C} the total number of cavities, N_{S} the total number of solenoids and T_{out} the output deuteron energy.

CM	CM1	CM2	CM3, 4 & 5
β	0.116	0.116	0.179
Seq.	8× (1S+1C)	5× (1S+2C) + (1S+1C)	4× (1S+2C) + (1S+1C)
N_{C}	8	11	9 × 3
N_{S}	8	6	5 × 3
T_{out} (MeV)	8.3	13.9	21.3, 30.3, 40

IFMIF/EVEDA accelerator in Rokkasho, Japan. From the RF perspective, the low-β HWRs and couplers are identical to the LIPAc one. Some of their mechanical features will be modified either to adapt them to the new overpressure protection envisioned (≈2 bar(a) Maximum Allowable Pressure) or to adapt their interfaces to the top loading assembly scheme of the DONES cryomodule as opposition to the side loaded assembly adopted for the Lipac cryomodule. Top loading offers several advantages like the reduction of the tooling required to insert the cavity string in the cryostat, the smaller footprint required in the assembly hall to perform the operation and the smaller number of mechanical interfaces to monitor during this critical operation. These positive aspects were observed and confirmed during the assembly of the top loaded SARAF cryomodules [54]. Regarding cryomodule transportation, two scenario are being analyzed, the case of the cryomodules transported fully assembled (#1) and the case of the cryomodules which are transported into two packages (#2), including a mechanical damping frame for the critical components (string of cavities and couplers). Experience from the SARAF HWR cryomodules [54] shows that that cryomodule 1 was successfully transported by plane and truck as two packages (case #2). The transportation frame of the cavity string and its top plate is shown on figure 23. If analyzed and designed early enough in the project, case #1 could offer many advantages (smaller number of operation at the DONES site) while providing mitigations to the critical transportation preparation steps. To complete this evaluation, a mechanical study accounting for transport accelerations is necessary to check the compatibility of the cryomodule transportation scheme with the final design of the cryomodules.

For the high-β cryomodule, a design and prototyping effort was led at CEA Saclay [55]. This naked high-β cavity prototype (figure 24) which has a 10 mm wider beam port diameter (50 mm), was manufactured by Zanon R&I. It was made from

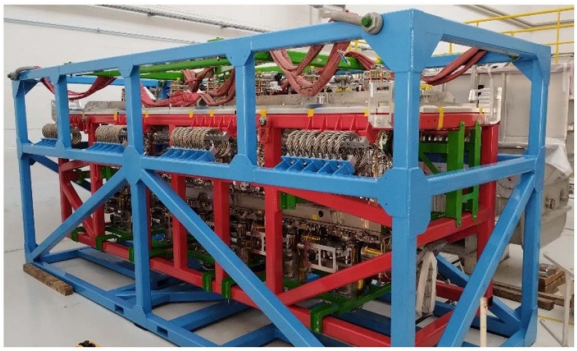

Figure 23. Damped transportation frame of the cavity string and top plate of the 1st SARAF cryomodule.

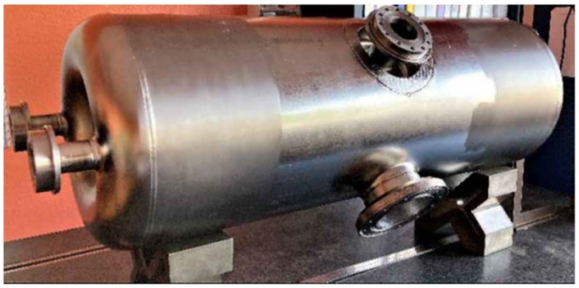

Figure 24. Prototype of a naked high-β cavity.

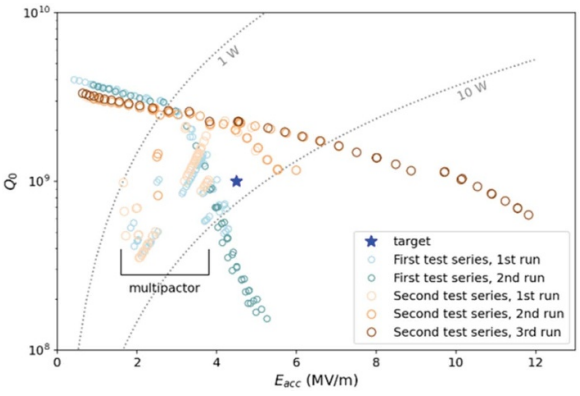

Figure 25. Vertical cryogenic tests without helium tank.

Nb sheets except for the central drift and beam tubes fabricated from blocks. It went through two series of vertical cryostat tests with successful results despite field emission due to surface pollution encountered during the first series of tests. As can be seen in figure 25, the cavity reached a 12 MV m^{-1} accelerating field without quenching and at nominal condition (4.5 MV m^{-1}) it reached a quality factor of 2.3×10^9 which is more than twice compared to the requirement. The next step is to add the helium tank to the cavity and check the capability of the SARAF like mechanical tuner to shift its central frequency. Preliminary warm tuner tests were successfully performed at the end of 2023 on the naked cavity demonstrating its ability to reach frequency shift greater than the expected 100 kHz.

Due to the greater diameter of this cavity, the interface for high-β coupler is 70 mm lower when compared to the

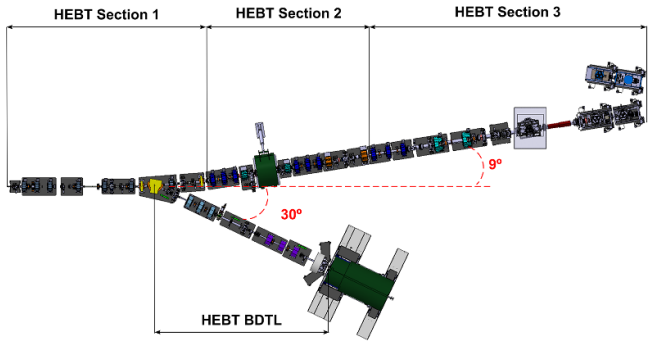

Figure 26. Mockup of the DONES HEBT.

low beta whereas the coupler body cannot shift further down without interfering with the RF transition box which is already close to the accelerator vault (AV) floor. Consequently, the high-β coupler antenna must be shortened accordingly and design studies will be led to optimize the coupling factor and check that the outer conductor is properly cooled in this new configuration.

3.5. *High-energy transport line*

The HEBT line (figure 26) is designed to ensure the beam meets the required footprint upon collision with the LT [56]. The main parameters for the footprint of the HEBT system are summarized in table 12. The HEBT has a secondary line, the BDTL, to deflect the beam from the target and dissipate its power with a HPBD. The BDTL will be used during the commissioning and start-up operations [57]. The 28 non-linear magnets (figure 27) shape the beam to deliver the requested footprint, whereas the two dipoles (figure 27) bend it by 9°.

Two shutters placed within the HEBT (figure 27) prevent back-scattering radiation during beam stop maintenance. A scraper (positioned in the middle of the HEBT, shown in figure 27) and a collimator remove the undesired halo beam and the particles diverted from the beam. In recent modifications, the collimator was moved closer to the target, meeting the 10 m proximity requirement, which required changing the collimator cooling fluid from water to liquid He [58].

By introducing a 77% aluminum-to-stainless steel ratio in all beam-facing elements, residual doses have decreased significantly through a minimized Co-56 production, allowing hands-on maintenance during beam stop periods [59]. High radiation areas are inaccessible to personnel, such as the RIR and the TIR. The precision manipulation and alignment of elements in those areas employ large replacement units (LRUs), pre-aligned boxes housing all elements, deployed via RH tools [60]. Mitigating accident risks, as described in [61], two fast isolation valves (FSIVs) are located within the RIR area, inside the AV. Enhanced by local shieldings [62], these protections ensure uninterrupted functionality of the FSIV throughout the demanding year-long service cycle, extending up to the annual maintenance period. The FSIV requires an inner gas atmosphere, which is provided by argon gas. The installation of a dedicated argon cabinet (see figure 27) inside the AV,

Table 12. Requirements of the HEBT&BD system.

Requirement	Target value
Particle type	D+
Beam energy	40 MeV
Beam emittance	0.3 π mm · mrad
Nominal beam peak current	125 mA
Nominal duty cycle	100 %
Nominal transmission ratio	>99.8 %
Achromatic bending	9°
Length SRF Linac—Target	48.8 m
Beam footprint at Li Target	$20 \times 5\,cm^2 (10 \times 5\,cm^2)$
BD peak power	5 MW
BD average power	<50 kW
RMS beam size at BD cone	∼40 mm
Divergence at BD cone	14–16 mrad
Off axis	<3 mm
Pressure at SRF Linac	$<5 \cdot 10^{-6}$ Pa
Pressure at Li Target	$<10^{-4}$ Pa

is foreseen to host the FSIV and the argon gas. Made of aluminum alloy to reduce residual doses, the argon cabinet has two access points: a ceiling entry for RH extraction to maintain the LRU containing both FSIV and a door for personnel to perform quick operations [58].

A cold trap is planned to be installed between the first dipole and the nearest quadrupole magnet of section 1 (see figure 27, but exact location pending) to protect the SRF LINAC cavities from evaporated lithium and other gases from the target.

Monitoring the beam footprint is crucial as it approaches the target, marking the final stage of the AS. The HEBT is equipped with essential diagnostic sensors, including: Current Transforms (CT), BPM and Beam Profile Chamber (BPC).

3.6. Beam diagnostics

The handling of such a powerful beam is not affordable without the full availability of a complete set of diagnostics which serve to tune and control the machine during all the commissioning and later operation phase. The main parameters to control during operation are: (1) the beam current, (2) the beam transverse and longitudinal centroid, (3) the transverse and longitudinal profile and (4) the beam losses. They are mainly focused in the transport control (section 3.6.1), in order to protect the machine and avoid machine activation, minimizing the machine downtime. Additional beam parameters are required to be identified during the commissioning phase, such as the beam emittance. A good qualification of those parameters is essential in order to optimize the acceleration in the superconducting structure or the matching with the RFQ.

3.6.1. Beam transport control. Several types of beam diagnostics are used to control the beam during the normal operation of the facility. The beam current is controlled mainly by current transformers: DC ones for CW operation, and AC for pulsed operations. In addition, a Fast version of the transformers is used to resolve the bunch structure as well as giving information of CW current in short bunch operation.

The beam losses were in principle going to be measured by ionization chambers as done in LIPAc along the transport lines. However, a new type of beam loss monitor, the neutron beam loss monitor (nBLM) [63], has been tested and integrated in the design. Developed by CEA in collaboration with ESS, this system is sensitive to fast neutrons produced by beam losses in the low energy parts of a hadron accelerator. It is based on Micromegas gaseous detectors, which can discriminate between gamma rays and signals produced by heavier particles. In the event of a beam loss, in the low energy region of a linear hadron accelerator, only neutrons and gamma rays escape. RF gamma rays can obscure the detection of actual beam losses, but Micromegas can distinguish between gamma rays and the ionization signals from neutrons, which are converted into alphas or protons. The nBLM system comprises two modules: a so-called fast module with a 100 ns response time for large losses, and a slow module with a delayed response due to neutron moderation but with an efficiency roughly 100 times greater than the fast module. Both modules operates in counting mode, with the same front end card, allowing being sensitive to small losses and they can switch to current mode in case of a high rate loss. Currently under commissioning at ESS [64], the system has also been tested at LINAC4 [63, 65], demonstrating its capability to detect small losses, with a better sensitivity than the BLM's based on ionization chambers. Additionally, the fast module can help identify the position of the loss. This year, nBLM modules have been tested at LIPAC. Preliminary results show a good response to deuterons losses also at low energy making the system adequate for DONES needs. Analysis of this data is on-going.

Inside the cryomodule, special beam loss detectors should be used, the so-called μLM. The performance of a scCVD diamond detector envisioned for the role of μBLMs was studied in mixed radiation environments and at cryogenic temperatures. As previously reported in [66], it was further confirmed that the charge collection efficiency of a diamond based detector decreased at cryogenic temperature by over 80% of its room temperature value for heavier ions such as helium (alpha particles), lithium and carbon [67]. This study was further expanded by evaluating the performance of the detector in neutron and γ-ray fields which more closely mimic the environment expected in the accelerator. It was found that the charge collection efficiency for γ-rays drops by 10% at 46 K while for neutrons it decreased to 50% by 80 K. Measuring the charge collection efficiency at 46 K in neutron fields was not possible as the signal was indistinguishable from the background noise. The drastic decrease in charge collection efficiency to neutrons and relatively small decrease to γ-rays present a challenge for neutron/γ-ray discrimination algorithms [68]. Methods to increase the charge collection efficiency of a diamond detector at cryogenic temperatures are currently being explored with very positive initial results. This would increase the effectiveness of discrimination algorithms and allow diamond detectors to function reliably as μBLM.

Another critical diagnostics to optimize the beam transport are the BPM's which measure the position of the beam centroid. The technology normally used is based in the pickup

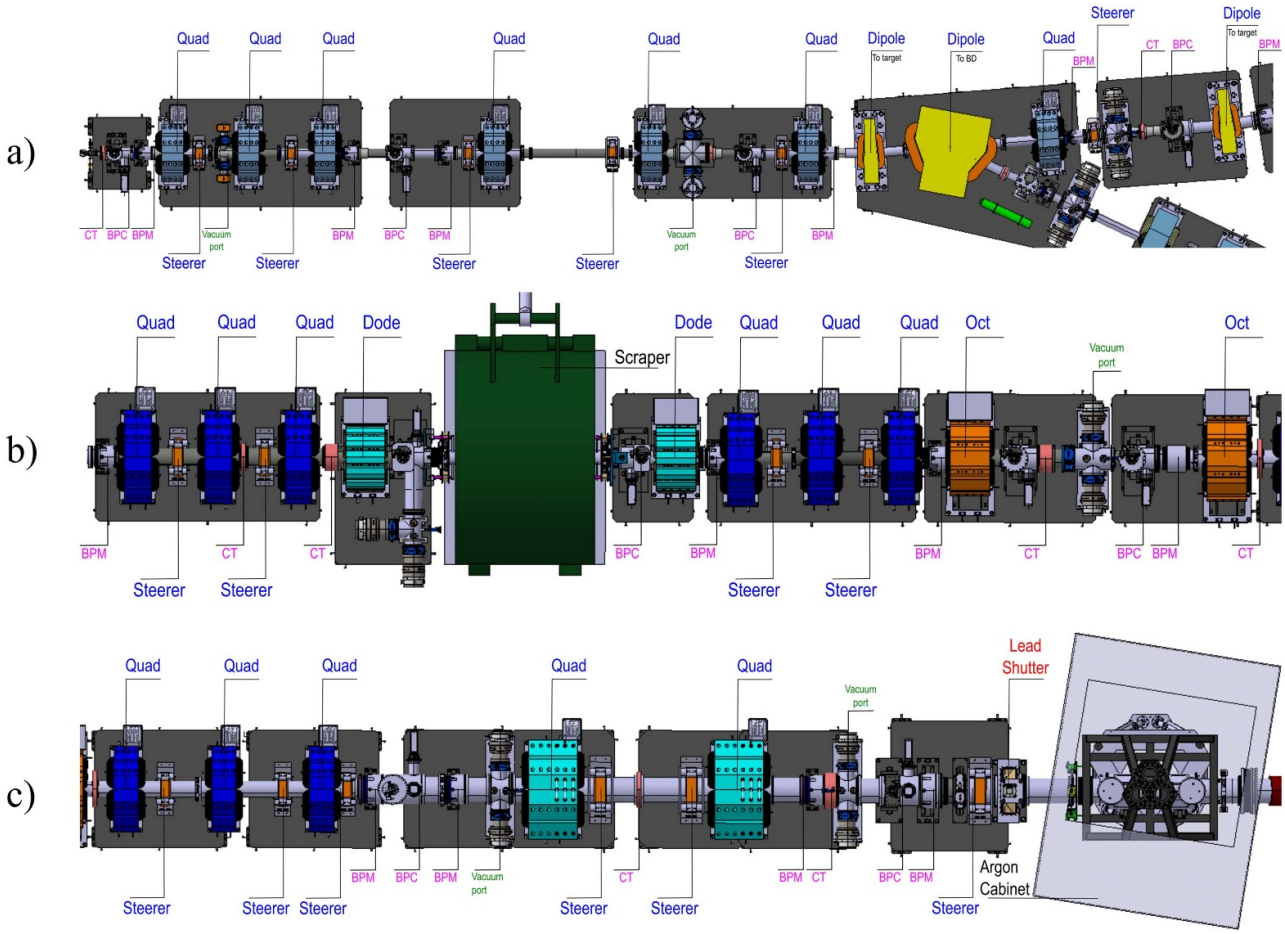

Figure 27. Sections 1 (*a*), 2 (*b*) and (3) of HEBT layout. The elements are: Magnets, Diagnostics and Vacuum, Shutter and stopper elements.

of the radiofrequency signal generated by the beam passing through the metallic beam pipe, which does not disturb the beam. Using this technology, an additional function is incorporated to the instrument: the measurement of the longitudinal position with respect to a master RF reference. In this way, the beam energy can be calculated and used for tuning of cavities or monitoring purposes along the line.

3.6.2. Characterization diagnostics. Transverse 2D phase space distributions, or transverse emittances, will be measured at IFMIF-DONES in the LEBT and MEBT to ensure that the beam phase space is matched to the acceptance criteria of the RFQ and SRF Linac accelerating structures. Another measurement location will be in the HEBT to characterize the beam before its interaction with the Lithium target.

- Emittance measurement in the LEBT. Allison type emittance scanners are high resolution scanners mostly used to measure the transverse emittance of ion beams at energies of tens of keV [69–73]. They have been selected for the LEBT of IFMIF-DONES. The Allison scanner of the LEBT of LIPAc is a single unit composed of a water cooled copper block made of two parts to form a front slit and covered with Tungsten tiles using HIP technique, two electrostatic deflecting plates, an electron repeller, a rear slit and a Faraday cup, see figure 28. This unit is scanned across one transverse plane of the beam with a stepper motor. At each stepper position, the beamlet passing through the front slit is swept across the rear slit by the deflecting plates and the beamlet current is measured by the Faraday cup. The Allison Scanner of LIPAc has been successfully commissioned at Rokkasho, Japan [74, 75]. For the nominal beam power of 15 kW (140 mA–100 keV D^+ beam + 10 mA of D_2^+ and D_3^+ ion species), transverse beam size and duty cycle must be carefully controlled to avoid deposition of too high power density. As a function of the beam diameter, the power density can reach more than 2 kW cm^{-2}. For beam density close to 2 kW cm^{-2}, simulations performed with COMSOL software show that the temperature can reach up to 1300 °C at the surface of the thermal shield made of Tungsten, leading to non negligible elastic deformation of the front slit due to thermal expansion and consequently to incorrect measurement. For this reason, the duty cycle must remain under 10% to decrease the average beam power and to ensure correct measurement even for small transverse beam size. The design of the Allison Scanner of LIPAc fulfill IFMIF-DONES requirements. However, the design will

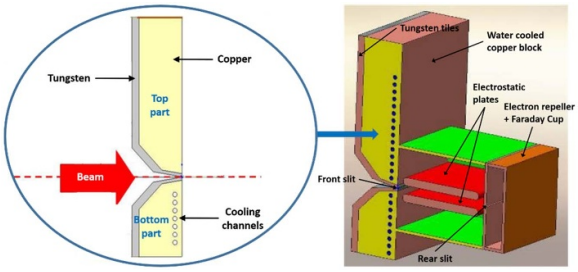

Figure 28. Allison scanner in the LEBT of LIPAc.

be improved in order to facilitate the alignment of each slit along their length.

- Emittance measurement in the MEBT/HEBT. In the MeV range, the majority of ion accelerators use other types of scanners, mostly double slit systems [76], slit-grid systems [77], slit-wire systems [78] or quadrupole scan technique [79]. For DONES, a slit-grid system has been chosen to be installed in a moveable diagnostic-plate that will be first placed downstream of the MEBT (phase B) and finally upstream of the HEBT (phases B+, C and D). This system has the advantage to allow also beam profile measurement using the SEM-Grids alone (slit in home position). The slit-grid system of LIPAc allows horizontal (H) and vertical (V) emittance measurement of a 125 mA D^+ beam up to an energy of 5 MeV (MEBT) and 9 MeV (HEBT). It is composed of two identical slits (H and V), of an electromagnetic steerer with two pairs of coils (H and V) and of a SEM-Grids with Tungsten wires in H and V planes, see figure 29. The slit is scanned across one transverse plane of the beam with a stepper motor, letting a beamlet traversing a drift of 1520 mm up to the SEM-Grid where the beamlet profile is measured. The steerer is used to increase the angular resolution of the measurement since the SEM-Grids has large wire gaps (1, 2 and 3 mm). The design of the slit of LIPAc is shown in figure 30. It is a water cooled copper block with teeth shape in front in order to decrease the beam power density. Layers, made of Graphite for the MEBT and of TZM for the HEBT (the latter to avoid sputtering and thus breakdown in the SRF Linac), are mounted with clamps in front of the copper block. Thermomechanical simulations show a negligible elastic displacement of the slit when subjected to the nominal high beam peak power of up to 1.125 MW (125 mA D^+ beam at 9 MeV) and for transverse beam sizes down to a sigma of 5 mm, by limiting the pulse length to 100 μs with a repetition rate of 1 Hz. The wires of the SEM-Grids have the same limitation in order to keep negligible the thermionic current. Using a 2.5 MeV H+ beam with current around 20 mA, comparisons between simulations and measurements performed downstream the MEBT of LIPAc show satisfying agreements [80]. Measurements performed with 5 MeV–125 mA D^+ beam, and I think with higher pulse length than 100 μs To show that the slit can sustain high beam power. For DONES, a similar design of slit-grid system will be adopted. For the HEBT of DONES, the energy is 40 MeV, thus probably not compatible with the slit (thermal stress).

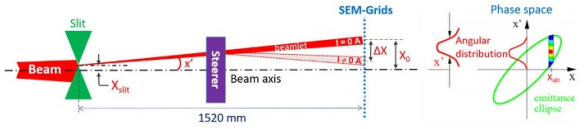

Figure 29. Principle of the beam emittance measurement at LIPAc using the slit-grid system.

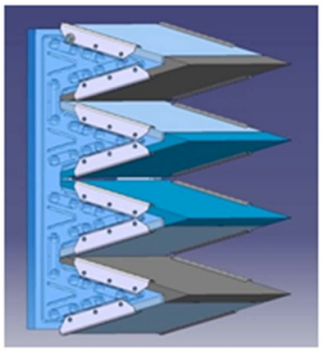

Figure 30. Design of the slit of LIPAc used for emittance measurement downstream the MEBT and the HEBT.

3.6.3. Target area diagnostics. One of the main focus of the accelerator development has been the control of the beam characteristics of the BOT. To ensure them, a good design of beam dynamics is not enough, but it is also capital to design beam diagnostics that characterize and monitor those characteristics in the real machine. The main objective is twofold: (1) characterization of the BOT to validate the beam dynamics, and (2) on-line monitoring to protect the target and associated beamline components from accidental events. Due to the high radiation near the target area, beam diagnostics are better placed in an area of lower radiation field. In this case, the room placed just before the TC area where the lithium is hosted, the so-called TIR. The TIR beamline components (or HEBT TIR section) are designed to ensure the desired parameters of the beam and lithium right before the beam hits the lithium target. This is achieved through diagnostics elements, as well as mechanical and safety devices. The HEBT TIR section is divided into two beamlines (primary and secondary beamline), each consisting of two separate modules which are also deemed large replaceable units. For the TIR, modular design was chosen to simplify the necessary RH operations due to high radiation doses. Inside the TIR all the components are going to be maintained via RH through the hatch on the ceiling of the room connected with the Access Cell. The primary beamline of the TIR hosts diagnostics for measurements of deuteron beam current, position, energy and profile and vacuum components. The aims are multiple: (1) checking of the exact position of the beam using BPMs, (2) tracking the shape of the beam using the BPC and (3) ensuring the HV levels within the entire TIR system. Using these elements, we have the final opportunity to control the beam parameters before the beam reaches the collimator where it will be shaped and focused. The secondary beamline elements will

host lithium diagnostics (such as cavity ring down spectroscopy, CRDS, or the lithium target thickness monitor based on laser method) [81], ensure necessary vacuum requirements and will also establish the upstream safety from activation by TC neutrons through shielding. Some of the beam diagnostics required a full research and development program. In particular, the beam profile monitoring is based on the prototypes developed for the LIPAc accelerator. Several experimental campaigns were past to improve the design, and to simulate similar operational conditions both theoretically and experimentally. Main candidates for the monitoring are light emission from the fluorescence of the beam with the lithium vapor, the argon or the optical transition radiation occurring at the interface point between the beam and the liquid lithium curtain.

3.7. RF power system

The IFMIF-DONES accelerator relies on a high-power RFPS to deliver a 175 MHz continuous wave (CW) signal to the accelerator cavities [82]. The required power at the cavity coupler interfaces is around 160 kW for the RFQ (eight couplers), around 12 kW for the re-buncher cavities (two couplers), a range between 40 kW and 70 kW for the low-β HWR cavities (nineteen couplers), and a range between 90 kW and 130 kW for the high-β HWR cavities (twenty-seven couplers). Therefore, the IFMIF-DONES RFPS has been designed with 56 RF stations capable of providing up to 200 kW, depending on the specific cavity requirement and the margins applied, resulting in a total RF output power exceeding 7 MW. Each RF station feeds a single cavity, except for the RFQ, which requires eight amplitude-phase balanced and synchronized RF stations acting as a unique source due to its high power demands (around 1.2 MW).

The IFMIF-DONES RFPS actively regulates the cavity field to compensate for various factors that can cause fluctuations, including beam loading, thermal expansion, and amplifier gain drift, using a fully digital low level RF (LLRF) control [83] that includes all the necessary feedback loops to control the accelerating voltage and protect the cavity subsystems. This ensures that the accelerating voltage remains within the specified limits of $\pm 1\%$ in amplitude and $\pm 1^\circ$ in phase, critical for optimal deuteron acceleration within the IFMIF-DONES accelerator. Although the nominal operation of the IFMIF-DONES accelerator is CW, the pulsed beam mode is being taken into account since the preliminary design phases due to its high importance for the accelerator commissioning, as demonstrated in LIPAc. The RF system can deliver a wide range of pulse parameters and the LLRF takes into account the specifics to tackle this even harder working mode.

3.7.1. Engineering design. Early on the IFMIF-DONES project, the decision to use a complete solid-state technology-based RF system was made. The conversion of the required 400 V, three-phase AC power (12 MVA total consumption) into the required RF power, is done in a two-step process. First, high-efficiency AC/DC converters (97% efficiency) provide a DC bias for the solid-state transistors, including active circuits for harmonics compensation (98% Power Factor Correction (PFC)). In the second step, Laterally-Diffused Metal-Oxide Semiconductor (LDMOS) transistors amplify the RF power achieving a DC-to-RF efficiency better than 70% and good reliability. Despite achieving a high global efficiency (better than 60%) during these conversions, up to 4.8 MW of heat will be generated in the RF Stations. This heat is dissipated using a dedicated cooling water system with a flow rate of around 550 m3/h at 25 °C, provided by the ASs Ancillaries. Depending on the cooling scheme of the final architecture, between 6.5% and 18.5% of this heat load could be released to the RF bay, imposing a considerable requirement to the building Heating, Ventilation, and Air Conditioning (HVAC) system.

The RFPS employs a two-level modular architecture, being the first level the RF station and the second one the amplifier modules (AMD) and the AC/DC power modules (ADPM). Using the same RF station architecture and the same sub-components for the complete system, mass scale cost reduction and high level of maintainability are guaranteed. Additionally, including the necessary amount of redundancy at the second level, the stringent 88% availability required for the IFMIF-DONES RFPS can be achieved. At the same time, a recent proposal for the reduction of the cooling water input temperature using a chiller, combined with an increased coolant flow, could provide a lower junction operating temperature that will increase the Mean Time Between Failures (MTBF) of the LDMOS transistors.

Reaching high power levels with Solid-State Power Amplifiers (SSPA) involves merging the outputs of multiple transistors. The conventional method uses a tree or corporate combining architecture, where several combining stages are sequentially arranged. The higher the power, the more combining stages are required, leading to higher overall combination losses and larger sizes. Alternatively, signal combination using a resonant RF cavity can provide a very efficient way to combine multiple radiofrequency power signals in a single step [84–86]. This innovative technique offers significant advantages over conventional corporate combiner schemes, while such traditional topology remains a viable option due to their proven design.

A simplified model of the RFPS architecture has been used to calculate the electrical consumption, the manufacturing cost, and the operating cost depending on the global efficiency achieved. The comparison between the minimum required efficiency of 60% and a supposed 65% system is shown in table 13. It shows that the increase of 5% in efficiency translates directly to a 1 MW smaller system, a 7 GW h yr^{-1} consumption saving and 2 kt yr^{-1} less carbon emissions. Related to costs, these implications mean that the RFPS would be 2 M€ cheaper to manufacture and the electric cost would be reduced by 1.1 M€ per year (taking into account 2022 power cost).

3.7.2. High-power SSPA stations. Due to the above-mentioned benefits of the resonant cavity combination, this technique has been selected for the development of a high-power RF Station prototype for the IFMIF-DONES RFPS. A

Table 13. Comparison between a 65% and a 60% efficiency RF power system. $\mu_{RF,G}$ is the global efficiency of the system, P_{req} the required power of the system, $E_{c,y}$ is the energy consumption per year, $M_{c,y}$ the mass of carbon emitted per year, $C_{c,y}$ the consumption cost per year and C_r the construction cost.

$\mu_{RF,G}$ %	P_{req} (MW)	$E_{c,y}$ (GW h)	$M_{c,y}$ (kt)	$C_{c,y}$ (M€)	C_r (M€)
60	11.8	94.7	27.2	15.1	58.0
65	10.9	87.4	25.2	14.0	56.1

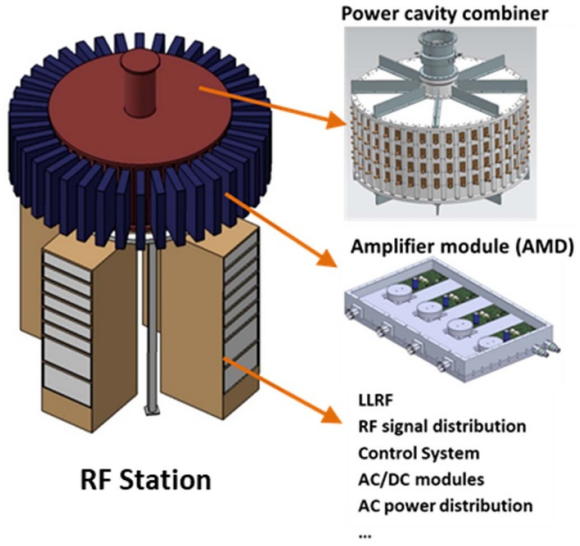

Figure 31. IFMIF-DONES RF station (architecture with 40 AMDs).

port-reconfigurable cavity combiner has been devised using a quasi-cylindrical forty-sided prism. The forty flat plates that form the cavity wall can either include or exclude input ports. In such a manner, the 56 IFMIF-DONES RF stations, with different output power requirements from 20 kW to 200 kW, can be implemented using the same combining device just modifying the number of amplifiers and input ports in the cavity combiner. This is advantageous in terms of flexibility, standardization for mass production, ease of spare parts acquisition, and maintainability. Figure 31 depicts an RF Station with 40 SS AMD connected to the cavity combiner. Each AMD has four outputs, which results in a total of 160 transistors and a 160-input cavity combiner. For a half-power RF Station, only 20 AMDs (80 transistors) would be required, that is, 20 plates with input ports and 20 blind plates. The other elements (LLRF, RF signal distribution, Control System, AC/DC modules, and AC power distribution) are located in the racks below the combiner and the AMDs.

A cavity combiner demonstrator has been developed to handle up to 240 kW at 175 MHz in the 160-input configuration. The measured combination efficiency has exceeded 99% with both small-signal and high-power tests at 100 kW CW [86]. Four additional AMDs to reach an enhanced 48 kW RF Station version have been fabricated and are currently under testing. Afterward, the RF Station prototype will be upgraded to its final configuration with 40 AMDs, resulting

Figure 32. Pictures of some components of the RF Station prototype: (*a*) cavity combiner in the CIEMAT RF Laboratory (*b*) 4×1.5 kW outputs SS Amplifier Module (AMD).

Figure 33. EIA 6″ 1/8 flexible coaxial line prototype.

in a 240 kW RF Station. The AMD measured performance reveals a high transistor efficiency of around 70%, thanks to an advanced cooling design that guarantees a low junction temperature and consequently better performance reliability to fulfill the availability requirements for IFMIF-DONES. Four additional AMDs will be available during Spring 2025, to reach an enhanced 48 kW RF Station version. The RF Station prototype will be upgraded to its final configuration with 40 AMDs by mid-2025, resulting in a 240 kW RF Station. The pictures of the cavity combiner testing and one of the AMDs are shown in figure 32.

Other innovative developments are being carried out, such as an EIA 6″ 1/8 flexible coaxial line prototype shown in figure 33. This component would be used in the interfaces between the RF Stations and the RF couplers of the accelerator cavities, placed at the end of the rigid coaxial lines. Its function is to absorb three-dimensional displacements provoked by thermal variations or tolerances while keeping low losses for efficient RF signal propagation. Apart from this main functionality, it also contributes to the simplification of the installation, replacement, and maintenance processes.

3.8. Ancillaries

The main function of the ASs ancillaries (ASA) is to provide all the utilities, equipment and resources to meet the needs of the IFMIF-DONES accelerator throughout its life cycle. This system adapts the plant services to the specific requirements of the ASs and consists of five subsystems in addition to its own LICS. The five subsystems are as follows: (1) water primary cooling loops, (2) electrical power distribution, (3) vacuum subsystem, (4) gas distribution subsystem and (5) cryoplant. The following sections describe the main characteristics of

these five subsystems, except for the vacuum one, which is described in section 2.2.

3.8.1. Conventional ancillaries. The water primary cooling loops, the electrical power distribution and the gas distribution subsystem are considered conventional auxiliaries and are described below. The water primary cooling loops of the accelerator are expected to manage a thermal load of approximately 8 MW. This subsystem consists of seven independent cooling units, each with autonomous systems to regulate water quality (such as conductivity and pH) as well as its main parameters (flow rate, pressure, temperature, etc). The unit that needs to dissipate the most thermal power is the one responsible for cooling the RF system. For most of the loops, the secondary side water comes directly from the plant services cooling towers (water temperature $\leqslant 27\,^{\circ}$C). However, for temperature control of specific components, such as the RFQ and re-buncher cavities, the cooled water is supplied by chillers. The RFQ cooling loop is of high importance as it is used to tune the cavity through temperature changes of $\pm 0.1\,^{\circ}$C. To accomplish this, the RFQ has two different manifolds and cooling circuits, warm and cold, each with three water inlets. The warm circuits have a dedicated pump and three-way valve for each inlet to ensure this restrictive tolerance. All water circuits cooling accelerator components close to the beam line are considered potentially contaminated. Among them, only the circuit cooling the Beam Dump cartridge should include a decay coil. This coil delays the arrival of water in the cooling machine room, ensuring that the water activation levels reach acceptable values.

The electrical installation to supply all the accelerator's needs is dimensioned to provide around 18 MVA in continuous operation. Among the different ASs, the RF Power Supply is clearly the largest consumer, requiring more than 80% of the accelerator's total power. The next largest consumers are mainly the cryoplant, the water primary cooling loops and the vacuum subsystem, whose consumptions are between 0.5 and 1 MVA. The IFMIF-DONES plant includes a Safety Energy Subsystem for the electrical supply of the safety important components (SIC). This system incorporates on-site emergency power sources such as diesel generators, uninterruptible power supplies (UPS's) and DC batteries. In this way, the distribution of electrical energy to the accelerator components is carried out through two clearly differentiated systems depending on whether the component is considered as SIC or Non-SIC. Non-SIC equipment is powered from a conventional electrical distribution subsystem. The great majority do not require an UPS, although, for those that do, an UPS powered from a conventional diesel generator is available. The IFMIF-DONES accelerator requires the following gases for its operation and maintenance: argon, helium, nitrogen and compressed air. In addition, it requires liquid nitrogen for cooling the Cold Box of the cryoplant, as described in the following section.

Argon will be used to purge the dry pumps of the vacuum subsystem and to vent the accelerator prior to maintenance or repair. Helium gas is required for vacuum leak testing and for cooling the beam collimator located at the end of the HEBT. For safety reasons, it was decided to avoid the use of water for collimator cooling. This is due to the proximity between the collimator and the lithium curtain of the target system and the risk that water could enter the beamline if the collimator were to break. Therefore, in the current design, the collimator is cooled with helium gas. Gaseous nitrogen is required for the operation and maintenance of the cryoplant, for both the oil removal system and the cold box. It is also planned to use nitrogen gas to vent the accelerator if needed. Finally, compressed air is necessary for the vacuum subsystem, maintenance of different accelerator components and pneumatic actuators.

3.8.2. Cryogenics. The main purpose of the cryogenic system of DONES is to fulfill all the cryogenic needs of the SRF LINAc. The required temperature of the cryomodules is 4.45 K in the Niobium superconducting cavities and 60 K for the insulating thermal shield. To achieve this liquid Helium has been selected as the cryogenic fluid. The liquefaction of Helium is achieved by a Claude cycle, in which seven stages of heat exchangers of the Cold Box will cool down the Helium down to supercritical conditions (6 K and 6 bar) and will be delivered through cryogenic pipes to the valve boxes where a Joule–Thomson valve will expand it and lower its temperature to the required 4.45 K. The Cold Box is equipped also with three turbines that will perform a Brayton cycle to extract power to compensate for the liquefaction load, the heat exchanger efficiency and any heat-in leaks. To cool down the thermal shield a line is extracted after the third heat exchanger and delivered to the valve box as gas He at 60 K. A simple schematic of the cryogenic system of DONES can be seen in figure 34.

The cryogenic system is also equipped with a liquid helium Dewar, placed between the Cold Box and the Valve Boxes, its purpose is to store the He in case of a malfunction of the cold box. The compressor station, located outside of the building, delivers the Helium in the required conditions for its usage in the Cold Box thanks as well to the oil removal system which ensures the cleanliness and purity of the fluid. Finally, the valve panels control the flow of GHe extracted from the phase separator which is used to cool down the power couplers and the current leads. The main cryo-distribution line is comprised of two lines (6 K and 60 K gas He) to feed the cryomodules through the valve boxes and to returning lines from them (4.5 K and 70 K gas He). Additionally, there are two more lines, one feeding the valve panels directly from the compressor station and the one returning from them (see figure 35). Each cryomodule has four different circuits that need to be cooled down, one for the superconducting cavities and solenoids, the outer conductor of the power couplers, the current leads and thermal shield. The cool down of each cryomodule is achieved in three different steps. The first step of the cryomodule cool down sequence is the cooling of the thermal shield and the cold mass together from 300 K (room temperature) to 60 K (the temperature of the high-pressure cold helium gas circuit supplied by the Cryoplant, already under operation). The control of the gas inlet temperature decrease will be processed by mixing cold gas (from 60 K line) and 300 K gas coming from HP line of the valve panels, once the gas is cold enough the HP

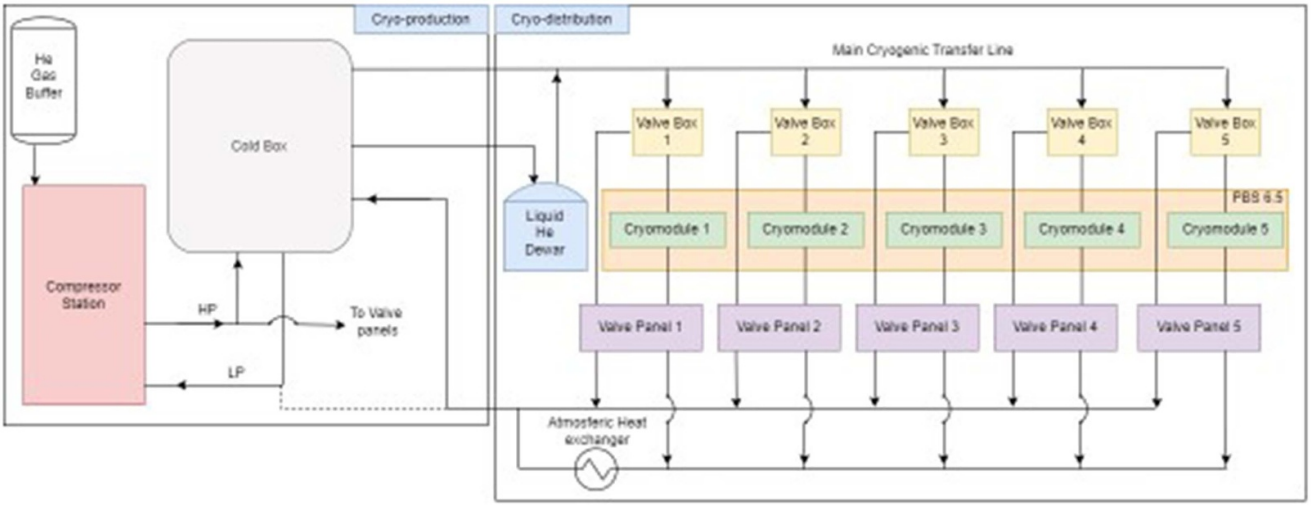

Figure 34. Block diagram of cryoplant showing the main components including the criodistribution and the connection with the SRF LINAC.

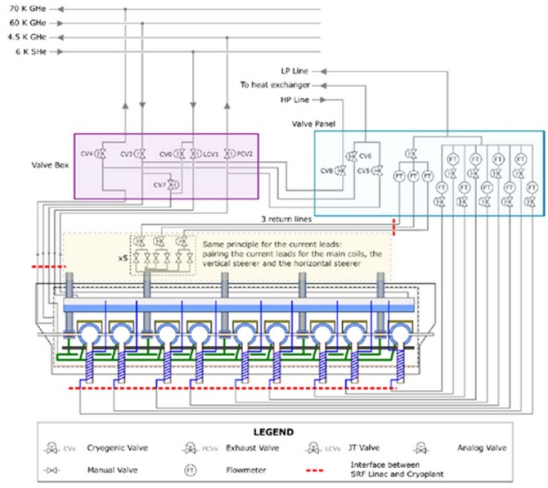

Figure 35. Detailed diagram developed by CEA of the cryogenic distribution for the high-β cryomodules (CM3, CM4 and CM5) with their valve boxes and valve panels.

line is closed. The second step begins once the cold mass temperature is around 60 K. The cold gas coming from the 60 K high pressure circuit is no more sent to the cavity string circuit, only to the thermal shield and the cold gas coming from the thermal shield is sent to the '70 K GHe' return line. To cool down the cold mass from 60 K down to a temperature close to the liquid helium temperature (4.45 K in the nominal operation of the cryomodule), the flow coming from the supercritical supply line (6 K SHe) is sent in the two inlet manifolds of the cavity string after being expanded through the valve. In this step the GHe is not returning by the line 4.5 K, it is returning through the valve panel to a heat exchanger. Finally, when the cryomodule reaches 5 K, the Joule Thomson valve is opened, and the gas Helium is returning by its proper line. The total cool down time has been estimated as 65 h. Additionally, the cryogenic system incorporates several safety devices. In the valve box there is a dedicated line with a spring relief valve in case of a sudden expansion of He. In the cryomodule there are pressure relief devices and burst discs are foreseen for the same purpose. The position of the exhausts of these devices are being studied to assess the risk of anoxia to maintenance operators in order to find the optimal positions of He discharges. Preliminary studies show that the risk is limited but deeper analyses will be conducted to confirm it.

4. Conclusion and outlook

The IFMIF-DONES driver accelerator is expected to become in few years one of the most intense and powerful hadron LINAC's in the world. This has imposed many challenges during the design phase, which have been overcome by the development of careful design analysis and prototyping work, led by many accelerator laboratories and institutions around the world. The design completed here represents the outcomes of many years of hard work, driven by the target inherent availability of the machine, with the common goal of providing to the international community a key facility in the roadmap to obtain electricity based on commercial fusion reactors in the next decades. Construction phase of the accelerator is already started from 2023. Components such as the transport lines, the RFQ or the injector are expected to launch their manufacturing during 2025. After ending the buildings construction by 2029, the first phase of the accelerator commissioning shall be ready to start in 2029, with beam on target in 2034. Accelerator shall be fully operational for the users by mid of 2030.

Acknowledgments

This work has been carried out partly within the framework of the EUROfusion Consortium (Grant Agreement No. 101052200—EUROfusion), and the DONES-ConP1 Consortium (Grant Agreement No. 101145952—DONES-ConP1), funded by the European Union via the Euratom Research and Training Programme, by the Regional

Andalousian Government under the Project TECHAC (ProyExcel_00989). Views and opinions expressed are however those of the author(s) only and do not necessarily reflect those of the European Union or the European Commission. Neither the European Union nor the European Commission can be held responsible for them.

ORCID iDs

I. Podadera https://orcid.org/0000-0002-3459-4631
M.J. Ferreira https://orcid.org/0000-0002-2141-5147
D. Jiménez-Rey https://orcid.org/0000-0003-1559-2179
C. de la Morena https://orcid.org/0000-0001-8470-4571
C. Torregrosa https://orcid.org/0000-0002-4322-8828
A. Ibarra https://orcid.org/0000-0002-2420-2497

References

[1] Ibarra A. *et al* 2018 *Nucl. Fusion* **58** 105002
[2] Podadera I. *et al* 2023 The IFMIF-DONES facility: a fusion-oriented 5 MW superconducting CW linear accelerator *Proc. IPAC'23* (*Int. Particle Accelerator Conf.* vol 14) (*Venice, Italy*, *7–12 May*) (JACoW Publishing) pp 2599–604
[3] Knaster J. *et al* 2015 *Nucl. Fusion* **55** 086003
[4] Cara P. *et al* 2016 The linear IFMIF prototype accelerator (LIPAC) design development under the European-Japanese Collaboration *Proc. IPAC'16* (*Int. Particle Accelerator Conf.* vol 7) (*Busan, Korea*, *8–13 May*) (JACoW Publishing) pp 985–8 (available at: https://jacow.org/ipac2016/papers/MOPOY057.pdf)
[5] Podadera I. *et al* 2024 *Nucl. Mater. Energy* **40** 101691
[6] Yee-Rendon B. 2022 Overview of ADS projects in the world *Proc. LINAC'22* (*Int. Linear Accelerator Conf.* vol 31) (*Liverpool, UK*, *28 August–2 September*) (JACoW Publishing) pp 310–3
[7] Champion M., Glens J., Stephens G., Galambos J., Moss J., White K., Connell M., Howell M., Evans N. and Kim S.H. 2024 Completion of the proton power upgrade project at the spallation neutron source *Proc. LINAC2024* (*Int. Linear Accelerator Conf.* vol 32) (*Chicago, USA*, *August*) (JACoW Publishing) pp 721–4 (available at: https://indico.jacow.org/event/71/contributions/5370)
[8] Xu S. *et al* 2023 *Nucl. Instrum. Methods Phys. Res. A* **1050** 168113
[9] Akagi T. *et al* 2024 Completion of Phase B+ beam commissioning of Linear IFMIF prototype accelerator (LIPAc) *Proc. LINAC2024* (*Int. Linear Accelerator Conf.* vol 32) (*Chicago, USA*, *August*) (JACoW Publishing) pp 698–701 (available at: https://indico.jacow.org/event/71/contributions/5351)
[10] Bargalló E. *et al* 2014 *Fusion Eng. Des.* **89** 2388–92
[11] Uriot D. and Pichoff N. 2015 Status of TraceWin code *Proc. IPAC'15* (*Richmond, USA*, *May*) (JACoW Publishing) pp 92–94 (available at: https://jacow.org/IPAC2015/papers/MOPWA008.pdf)
[12] Nghiem P., Chauvin N., Comunian M., Delferrière O., Duperrier R., Mosnier A., Oliver C. and Uriot D. 2011 *Nucl. Instrum. Methods Phys. Res. A* **654** 63–71
[13] Nghiem P., Chauvin N., Comunian M., Oliver C., Simeoni W., Uriot D. and Valette M. 2014 *Laser Part. Beams* **32** 639–49
[14] Delferrière O., De Menezes D., Gobin R., Harrault F. and Tuske O. 2008 *Rev. Sci. Instrum.* **79** 02B723
[15] Spädtke P. INP 1998 Axcel version 3.43
[16] Kalvas T., Tarvainen O., Ropponen T., Steczkiewicz O., Ärje J. and Clark H. 2010 *Rev. Sci. Instrum.* **81** 02B703
[17] Gerardin F. 2018 Etude de la compensation de charge d'espace dans les lignes basse énergie des accélérateurs d'ions légers de haute intensité *Theses*
[18] Bellan L. 2018 Beam dynamics characterization of the IFMIF/EVEDA RFQ input beam *PhD Thesis* Università di Padova (available at: http://hdl.handle.net/11577/3425290)
[19] Grote D.P., Friedman A., Vay J. and Haber I. 2005 *AIP Conf. Proc.* **749** 55–58
[20] Winklehner D. and Leitner D. 2015 *J. Instrum.* **10** T10006
[21] Bellan L. *et al* 2022 *J. Phys.: Conf. Ser.* **2244** 012078
[22] Comunian M., Fagotti E., Pisent A. and Posocco P.A. 2008 Beam dynamics of the IFMIF-EVEDA RFQ *Proc. EPAC'08* (*European Particle Accelerator Conf.* vol 11) (Genoa, Italy) (JACoW Publishing) pp 3536–8 (available at: https://jacow.org/e08/papers/THPP075.pdf)
[23] Crandall K.R. and Wangler T.P. 1988 *AIP Conf. Proc.* **177** 22–28
[24] Comunian M., Pisent A. and Fagotti E. 2008 The IFMIF-EVEDA RFQ: beam dynamics design *Proc. LINAC'08* (*Linear Accelerator Conf.* vol 24) (*Victoria, Canada*, *29 September–3 October*) (JACoW Publishing) pp 145–7 (available at: https://jacow.org/LINAC08/papers/MOP036.pdf)
[25] Comunian M., Bellan L. and Pisent A. 2024 *J. Instrum.* **19** P01024
[26] Chauvin N., Duperrier R.D., Mosnier A., Nghiem P.A.P. and Uriot D. 2009 Optimization results of beam dynamics simulations for the superconducting HWR IFMIF linac *Proc. PAC'09* (*Particle Accelerator Conf.* vol 23) (*Vancouver, Canada*, *May*) (JACoW Publishing) pp 3193–5 (available at: https://jacow.org/PAC2009/papers/TH5PFP005.pdf)
[27] Kennedy J. and Eberhart R. 1995 Particle swarm optimization *Proc. ICNN'95—Int. Conf. on Neural Networks* vol 4 pp 1942–8
[28] Jameson R., Ferdinand R., Klein H., Rathke J., Sredniawski J. and Sugimoto M. 2004 *J. Nucl. Mater.* **329–333** 193–7
[29] Poljak D. and Susnjara A. 2023 *Deterministic and Stochastic Modeling in Computational Electromagnetics: Integral and Differential Equation Approaches* (Wiley)
[30] Poljak D., Oliver C., Chauvin N., Podadera I. and Tadic T. 2024 Sensitivity analysis (SA) of the uncertainty propagation (UP) in static and dynamic simulations of beam profile at the IFMIF-DONES beam dump *Proc. SOFT 2024*
[31] Chauvin N., Bazin N., Chel S., Du L. and Plouin J. 2019 Beam dynamics errors studies for the IFMIF-DONES SRF-LINAC *Proc. IPAC'19* (*Melbourne, Australia*, *May*) (JACoW Publishing) pp 3103–5 (available at: http://accelconf.web.cern.ch/ipac2019/papers/WEPTS010.pdf)
[32] Pérez C.C., Ferreira M.J., Hauer V., Podadera I., Sabogal A., Herranz D.S. and Torregrosa C. 2025 *Vacuum* **234** 114091
[33] Hauer V. and Day C. 2018 *Fusion Eng. Des.* **136** 1063–7
[34] Kersevan R. and Ady M. 2019 Recent developments of Monte-Carlo codes Molflow+ and Synrad+ *Proc. IPAC'19* (*Melbourne, Australia*, *May*) (JACoW Publishing) pp 1327–30 (available at: http://accelconf.web.cern.ch/ipac2019/papers/TUPMP037.pdf)
[35] Torregrosa-Martín C., Martín-Fuertes F., Marugán J.C., Qiu Y. and Ibarra A. (the EUROfusion WPENS Team) 2025 *Nucl. Fusion* **65** 122009
[36] Dalesio L.R. *et al* 2017 EPICS 7 provides major enhancements to the EPICS toolkit *Proc. ICALEPCS'17* (*Barcelona, Spain*, *October*) (JACoW Publishing) pp 22–26 (available at: https://jacow.org/icalepcs2017/papers/MOBPL01.pdf)

[37] Gaubert G. *et al* 2015 *High Intensity ECR ion Source: SILHI From Research to Industry* (Bhabha Atomic Research Centre)

[38] Sun L.T. 2013 High intensity operation for heavy ion cyclotron of highly charged ECR ion sources *Proc. Cyclotrons'13* (*Vancouver, Canada*, *September*) (JACoW Publishing) pp 125–9 (available at: https://jacow.org/CYCLOTRONS2013/papers/TU1PB01.pdf)

[39] Wu W. *et al* 2020 *Vacuum* **182** 109744

[40] Arianer J. and Geller R. 1981 *Annu. Rev. Nucl. Part. Sci.* **31** 19–51

[41] Geller R. 1990 *Annu. Rev. Nucl. Part. Sci.* **40** 15–44

[42] Abal J. *et al* 2013 *Fusion Eng. Des.* **88** 2535–8

[43] Gobin R., Beauvais P.-Y., Delferrière O., De Menezes D., Tuske O., Adroit G., Gauthier Y. and Harrault F. 2008 *Rev. Sci. Instrum.* **79** 02B303

[44] Bolzon B., Chavin N. and Chel S. 2023 List of potential improvements based on LIPAc operational feedback *Technical Report* (EUROfusion)

[45] Pisent A. 2010 RFQ for CW applications *Proc. LINAC'10* (*Linear Accelerator Conf.* vol 25) (*Tsukuba, Japan*, *September*) (JACoW Publishing) pp 372–6 (available at: https://jacow.org/LINAC2010/papers/TU301.pdf)

[46] Pisent A., Grespan F. and Palmieri A. 2008 RF design of the IFMIF-EVEDA RFQ *Proc. LINAC'08* (*Linear Accelerator Conf.* vol 24) (*Victoria, Canada*, *September–October*) (JACoW Publishing) pp 148–50 (available at: https://jacow.org/LINAC08/papers/MOP037.pdf)

[47] Palmieri A., Grespan F. and Pisent A. 2017 Tuning the IFMIF 5MeV RFQ accelerator *Proc. LINAC'16* (*Linear Accelerator Conf.* vol 28) (*East Lansing, USA*, *September*) (JACoW Publishing) pp 969–71 (available at: https://jacow.org/linac2016/papers/THPLR049.pdf)

[48] Pisent A. *et al* 2008 IFMIF-EVEDA RFQ design *Proc. EPAC'08* (*European Particle Accelerator Conf.* vol 11) (*Genoa, Italy*, *May*) (JACoW Publishing) pp 3542–4 (available at: https://jacow.org/e08/papers/THPP078.pdf)

[49] Pisent A., Grespan F., Palmieri A. and Scantamburlo F. 2010 3D aspects of the IFMIF-EVEDA RFQ: design and optimization of the vacuum grids, of the slug tuners and of the end cell *Proc. LINAC'10* (*Linear Accelerator Conf.* vol 25) (*Tsukuba, Japan*, *September*) (JACoW Publishing) pp 533–5 (available at: https://jacow.org/LINAC2010/papers/TUP055.pdf)

[50] Pepato A. *et al* 2010 Engineering design and first prototype tests of the IFMIF-EVEDA RFQ *Proc. IPAC'10* (*Kyoto, Japan*, *May*) (JACoW Publishing) pp 600–2 (available at: http://accelconf.web.cern.ch/IPAC10/papers/MOPEC060.pdf)

[51] Scantamburlo F. 2013 Design and analysis of a RFQ resonant cavity for the IFMIF project *Theses*

[52] Dima R. *et al* 2013 Present status and progresses of RFQ of IFMIF/EVEDA *Proc. IPAC'13* (*Shanghai, China*, *May*) (JACoW Publishing) pp 2729–31 (available at: https://jacow.org/IPAC2013/papers/WEPFI014.pdf)

[53] Bazin N. and Chel S. 2022 Cryomodule development for the materials irradiation facility: from IFMIF-EVEDA to IFMIF-DONES *Proc. SRF'21* (*Int. Conf. on RF Superconductivity* vol 20) (*East Lansing, USA*, *27 June–2 July*) (JACoW Publishing) p 534 (available at: https://jacow.org/srf2021/papers/WEPFAV001.pdf)

[54] Pichoff N. *et al* 2023 The SARAF-linac project status *Proc. IPAC'23* (*Int. Particle Accelerator Conf.* vol 14) (JACoW Publishing) pp 2313–5

[55] Plouin J. *et al* 2023 Design, fabrication and test of a 175 MHz, $\beta = 0.18$, half wave resonator for the IFMIF-DONES SRF-Linac *Proc. SRF'23* (*Int. Conf. on RF Superconductivity* vol 21) (JACoW Publishing) pp 477–9

[56] Nomen O. *et al* 2020 *Fusion Eng. Des.* **153** 111515

[57] Sánchez-Herranz D. *et al* 2022 Status of the engineering design of the IFMIF-DONES high energy beam transport line and beam dump system *Proc. IPAC'22* (*Int. Particle Accelerator Conf.* vol 13) (*Bangkok, Thailand*, *12–17 June*) (JACoW Publishing) pp 2520–3 (available at: https://jacow.org/IPAC2022/papers/THPOST035.pdf)

[58] Macià L. *et al* 2024 *Fusion Eng. Des.* **202** 114312

[59] Ogando F., Macia L., Lopez V., Podadera I. and Sanchez-Herranz D. 2024 *Nucl. Mater. Energy* **38** 101592

[60] Sánchez-Herranz D., Nomen O., Arranz F., Coloma S., Podadera I. and Varela R. 2021 *Fusion Eng. Des.* **168** 112636

[61] Sabogal A. *et al* 2023 Multipurpose vacuum accident scenarios (MuVacAS) prototype for the IFMIF-DONES linear accelerator *Proc. IPAC'23* (*Int. Particle Accelerator Conf.* vol 14) (JACoW Publishing) pp 4324–7

[62] Lopez-Revelles A., Ogando F., Lopez V., Torregrosa C., Macia L., Podadera I. and Sanz J. 2024 *Fusion Eng. Des.* **202** 114385

[63] Segui L. *et al* 2023 *J. Instrum.* **18** P01013

[64] Kittelmann I.D., Boutachkov P., Effinger E., Grishin V., Lernevall A., Viganò W. and Zamantzas C. 2023 Detector response studies of the ESS ionization chamber *Proc. 12th Int. Beam Instrum. Conf. (IBIC'23)* (*Int. Beam Instrumentation Conf.* vol 12) (*Saskatoon, Canada*, *10–14 September*) (JACoW Publishing) pp 183–6 (available at: https://jacow.org/ibic2023/papers/tup004.pdf)

[65] Dolenc Kittelmann I. *et al* 2022 *Phys. Rev. Accel. Beams* **25** 022802

[66] Jansen H. 2015 Chemical vapour deposition diamond: charge carrier movement at low temperatures and use in time-critical applications *PhD Thesis* Rheinische Friedrich-Wilhelms-Universität Bonn (available at: https://hdl.handle.net/20.500.11811/6405)

[67] Cosic D., Provatas G., Jaksic M. and Begusic D. 2022 *Diam. Relat. Mater.* **127** 109184

[68] Cosic D., Provatas G., Jakšić M. and Begusic D. 2024 *IEEE Trans. Instrum. Meas.* **73** 1–10

[69] Allison P.W., Holtkamp D.B. and Sherman J.D. 1983 An emittance scanner for intense low-energy ion beams *Proc. PAC'83* (JACoW Publishing) pp 2204–7

[70] Stockli M.P., Welton R.F., Keller R. and Leitner M. 2006 *Rev. Sci. Instrum.* **77** 03B706

[71] Dombsky M., Baartman R., Bricault P., Doornbos J., Jayamanna K., Kuo T., Mackenzie G., McDonald M., Schmor P. and Yuan D. 1998 *Rev. Sci. Instrum.* **69** 1170–2

[72] Kim Y.J., Hong I.S., Kim H.S. and Hwang Y.S. 2004 *Rev. Sci. Instrum.* **75** 1681–3

[73] Lim E.H., Kwon J.W., Chung Y.S., Woo H.J., Kim G.D. and Kim E.S. 2023 *Rev. Sci. Instrum.* **94** 085111

[74] Bolzon B. *et al* 2015 Beam diagnostics of the LIPAC injector with a focus on the algorithm developed for emittance data analysis of high background including species fraction calculation *Proc. IBIC'15* (*Melbourne, Australia*, *September*) (JACoW Publishing) pp 313–7 (available at: https://jacow.org/IBIC2015/papers/TUPB008.pdf)

[75] Bolzon B. *et al* 2018 *Fusion Eng. Des.* **136** 1300–5

[76] Yu L., Sui Y.F., Zhao J.X. and Zhu D.C. 2016 Design and application of double-slit emittance meter for C-ADS

proton beams *Proc. IPAC'16* (*Int. Particle Accelerator Conf.* vol 7) (JACoW Publishing) pp 164–6 (available at: https://jacow.org/ipac2016/papers/MOPMB034.pdf)

[77] Cheymol B., Bravin E., Dutriat C. and Lefévre T. 2009 Design of a new emittance meter for LINAC4 *Proc. DIPAC'09* (*Basel, Switzerland*, *May*) (JACoW Publishing) pp 396–8 (available at: https://jacow.org/d09/papers/TUPD42.pdf)

[78] Dumas J. *et al* 2023 SARAF beam commissioning results: injector, MEBT *Proc. IPAC'23* (*Int. Particle Accelerator Conf.* vol 14) (JACoW Publishing) pp 1703–5

[79] Hong-Ping J. *et al* 2014 *Chin. Phys. C* **38** 087002

[80] Marroncle J. *et al* 2019 Transverse emittance measurement of a 2.5 MeV proton beam on LIPAc, IFMIF'S prototype *Proc. IBIC'19* (*Malmö, Sweden*, *September*) (JACoW Publishing) pp 288–92 (available at: https://jacow.org/ibic2019/papers/TUPP006.pdf)

[81] Nitti F., Maestre J., Dezsi T., Gordeev S., Holstein N., Brenneis B., Buligins L., Molla J. and Ibarra A. 2025 *Nucl. Fusion* **65** 122004

[82] Regidor D., de la Morena C., Iriarte D., Sierra F., Dragaš S., Marini P., Sanz J., Molla J. and Ibarra A. 2021 *Fusion Eng. Des.* **167** 112322

[83] de la Morena C. *et al* 2018 *IEEE Trans. Nucl. Sci.* **65** 514–22

[84] de la Morena C., Regidor D., Lara A., Iriarte D., Sierra F., García F., Weber M., Molla J. and Ibarra A. 2020 *Nucl. Instrum. Methods Phys. Res. A* **972** 164108

[85] de la Morena C., Regidor D., Iriarte D., Sierra F., Ugarte E., Dragaš S., Marini P., Molla J. and Ibarra A. 2021 *Fusion Eng. Des.* **168** 112396

[86] de la Morena C., Regidor D., Iriarte D., Ugarte E., Dragaš S., Martínez A., Molla J. and Ibarra A. 2023 *Fusion Eng. Des.* **189** 113475